On-Orbit Degradation of Solar Instruments

A. BenMoussa · S. Gissot · U. Schühle · G. Del Zanna · F. Auchère · S. Mekaoui ·
A.R. Jones · D. Walton · C.J. Eyles · G. Thuillier · D. Seaton · I.E. Dammasch ·
G. Cessateur · M. Meftah · V. Andretta · D. Berghmans · D. Bewsher · D. Bolsée ·
L. Bradley · D.S. Brown · P.C. Chamberlin · S. Dewitte · L.V. Didkovsky ·
M. Dominique · F.G. Eparvier · T. Foujols · D. Gillotay · B. Giordanengo · J.P. Halain ·
R.A. Hock · A. Irbah · C. Jeppesen · D.L. Judge · M. Kretzschmar · D.R. McMullin ·
B. Nicula · W. Schmutz · G. Ucker · S. Wieman · D. Woodraska · T.N. Woods

Abstract We present the lessons learned about the degradation observed in several space
solar missions, based on contributions at the Workshop about On-Orbit Degradation of Solar

A. BenMoussa · D. Bolsée · B. Nicula
Solar Terrestrial Centre of Excellence, 1180 Brussels, Belgium

A. BenMoussa
e-mail: ali.benmoussa@stce.be

A. BenMoussa · S. Gissot (✉) · D. Seaton · I.E. Dammasch · D. Berghmans · M. Dominique ·
B. Giordanengo · B. Nicula
Royal Observatory of Belgium, 1180 Brussels, Belgium
e-mail: samuel.gissot@oma.be

U. Schühle
Max-Planck-Insitut für Sonnensystemforschung, 37191 Katlenburg-Lindau, Germany

G. Del Zanna
DAMTP – Centre for Mathematical Sciences, University of Cambridge, Wilberforce Road, Cambridge
CB3 0WA, UK

F. Auchère
Institut Astrophysique Spatiale, CNRS-Université Paris-Sud 11, 91405 Orsay, France

S. Mekaoui
European Commission – Joint Research Centre, Ispra, Italy

S. Mekaoui · S. Dewitte
Royal Meteorological Institute of Belgium, 1180 Brussels, Belgium

A.R. Jones · F.G. Eparvier · C. Jeppesen · G. Ucker · D. Woodraska · T.N. Woods
Laboratory for Atmospheric and Space Physics, University of Colorado, Boulder, CO, USA

D. Walton · L. Bradley
Mullard Space Science Laboratory, Holmbury St. Mary, Dorking, Surrey, RH5 6NT, UK

Ⲽ Springer

and Space Weather Instruments that took place at the Solar Terrestrial Centre of Excellence (Royal Observatory of Belgium) in Brussels on 3 May 2012. The aim of this workshop was to open discussions related to the degradation observed in Sun-observing instruments exposed to the effects of the space environment. This article summarizes the various lessons learned and offers recommendations to reduce or correct expected degradation with the goal of increasing the useful lifespan of future and ongoing space missions.

1. Introduction

Investigating and analyzing the degradation of space instruments are crucial parts of achieving the scientific goals of all such instruments. Remote–sensing instrumentation exposed to

C.J. Eyles
Space Science and Technology Department, Rutherford Appleton Laboratory, Chilton, Didcot, UK

C.J. Eyles
Grupo de Astronomia y Ciencias del Espacio, ICMUV, Universidad de Valancia, Valencia, Spain

G. Thuillier · M. Meftah · T. Foujols · A. Irbah
LATMOS-CNRS UMR 8190, Université Paris VI, Université de Versailles, Versailles, France

G. Cessateur · W. Schmutz
PMOD/WRC, Dorfstr 33, Davos, 7260, Switzerland

V. Andretta
INAF, Osservatorio Astronomico di Capodimonte, Salita Moiariello, 16, 80141 Naples, Italy

D. Bewsher · D.S. Brown
Jeremiah Horrocks Institute, University of Central Lancashire, Preston, UK

D. Bolsée · D. Gillotay
Belgium Institute for Space Aeronomy, 1180 Brussels, Belgium

P.C. Chamberlin
Goddard Space Flight Center, Greenbelt, MD, USA

L.V. Didkovsky · D.L. Judge · S. Wieman
Space Sciences Center, University of Southern California, Los Angeles, CA, USA

J.P. Halain
Centre Spatial de Liège, Université de Liège, Liège Science Park, 4013 Angleur, Belgium

R.A. Hock
Air Force Research Laboratory, Kirtland Air Force Base, Alburqueque, NM, USA

M. Kretzschmar
LPC2E/CNRS, (UMR 7328), Université d'Orléans, 45071 Orléans cedex 2, France

D.R. McMullin
Space Systems Research Corporation, 1940 Duke Street 200, Alexandria, VA 22314, USA

Table 1 Solar space instruments used. The acronyms used in this table are defined in their corresponding section.

Mission/instrument	Telescope (T) Spectrometer (S) Radiometer (R)	Spectral range [nm]	Mission length (... – present)
SOHO/SUMER	T–S	66 – 161	Dec. 1995
SOHO/CDS	S	15 – 79	Dec. 1995
SOHO/EIT	T	17 – 30	Dec. 1995
SOHO/CELIAS-SEM	R–S	0.1 – 50	Dec. 1995
SOHO/DIARAD	R	Total Solar Irradiance	Dec. 1995
Hinode/EIS	T–S	17 – 29	Sep. 2006
STEREO/HI1A HI1B	T	630 – 730	Oct. 2006
ISS/SOLSPEC	R–S	165 – 3080	Feb. 2008
PROBA2/SWAP	T	17.4	Nov. 2009
PROBA2/LYRA	R	0.1 – 70, 121.6, 190 – 222	Nov. 2009
SDO/EVE: EPS, MEGSA1-A2-B-P	R–S	0.1 – 105, 121.6	Feb. 2010
Picard/PREMOS	R	210, 215, 266, 535, 607, 782	June 2010
Picard/SODISM	T	215, 393, 535, 607, 782	June 2010

the space environment usually degrades due to the harsh environment in which the instruments are expected to operate. Solar instruments – telescopes, spectrographs and radiometers – are particularly vulnerable because their optical elements are exposed to unshielded solar radiation. For example, these instruments have historically suffered substantial degradation due to a combination of solar irradiation and instrumental contamination that can cause polymerization of organic material and, subsequently, irreversible deposition of this material on the instruments' optical surfaces.

Different methods and approaches have been used to assess and monitor the evolution of these instruments' degradation. To reach a better understanding of how to both monitor and study this degradation, the Solar Terrestrial Centre of Excellence (STCE) at the Royal Observatory of Belgium organized a workshop on this subject on 3 May 2012 in Brussels, Belgium. Representatives from several active space-based solar instruments (see Table 1) contributed to this workshop.

In this article we present analyses of these instruments' degradation (or non-degradation), the causes of degradation when they could be identified, the consequences of degradation, and methods by which the impact of degradation can be mitigated. We also provide a summary of the lessons learned and recommendations for best practices with the hope that this information will help scientists and engineers to prevent – or cope with – degradation of active and future space-based solar instruments.

2. Solar Instruments Onboard SOHO

The *Solar and Heliospheric Observatory* (SOHO: Fleck, Domingo, and Poland, 1995) is a successful solar mission that includes – among other instruments – radiometers, spectrometers, and an extreme-ultraviolet (EUV) imager. It has operated for more than 16 years at the Lagrangian L_1 point. SOHO was launched in December 1995 and began routine operations in January 1996. At the beginning of the development phase of SOHO, the degradation

processes were analyzed and appropriate procedures and design concepts were developed to eliminate them. During the design phase of SOHO's instruments and spacecraft, a meticulous cleanliness program was implemented to control molecular and particle contamination (Pauluhn, Huber, and von Steiger, 2002). A substantial part of the success of SOHO is due to the thoughtful design of the spacecraft, payload module, instruments, and a strict material-selection process.

2.1. Cleanliness and Calibration Stability of the SUMER Spectrograph

Among the suite of remote-sensing instruments onboard SOHO are three spectrographs operating in the vacuum and extreme ultraviolet (VUV–EUV) range. The *Solar Ultraviolet Measurements of Emitted Radiation* (SUMER) instrument is a telescope/spectrometer. The detailed design has been described by Wilhelm *et al.* (1995). In brief, it consists of a single telescope mirror and a spectrograph. The reflective optics, the telescope mirror, the collimator and wavelength scan mirror, and the grating are made of silicon carbide. The spectrograph carries two detectors with an instantaneous spectral range of 4 nm in first order (the second-order spectrum is superposed). A wavelength-scanning mechanism selects the displayed spectral band in the range from 66 up to 161 nm.

2.1.1. Cleanliness Program

During the design phase of SUMER, a thorough cleanliness control program was implemented (Schühle, 1993). The cleanliness requirements were estimated by model calculations of contaminants on the optical system. Particle fallout rates in cleanrooms published at that time were used to calculate the exposure time of the flight hardware inside the cleanroom environments. With the results of the studies, a cleanliness-control plan was established that contains the cleanliness requirements, handling practices for all hardware, as well as the control procedures and verification of cleanliness. The main features of the cleanliness program, however, were cleanliness design, material selection, cleaning, and bake-out for space conditioning.

2.1.2. Cleanliness Design

The SUMER structural housing is made of aluminum that was thoroughly cleaned and hermetically sealed when it was assembled. Only an aperture-door mechanism was able to open the optical compartment to the environment at any time of the assembly, integration, tests, and validation phases. The spring-loaded door lid provided the functionality of a valve that opens during launch for depressurization. A transparent window inside the door lid provided heat input by the Sun to the primary mirror when the door was closed. In this way, the primary mirror stays the hottest element inside the instrument. Internally, the telescope and spectrograph form two compartments separated by walls containing the spectrograph entrance slit. The two compartments were connected by large venting holes to avoid a pressure difference between them and to prevent gas flowing through the slit. There are as few electronic components inside the housing as possible. In addition to the optics, the mechanical driving mechanisms contain ultra-high vacuum motors and position encoders, temperature sensors, and limit switches. To deflect the majority of the solar-wind particles, deflector plates are implemented inside the entrance baffle, far ahead of the mirror.

2.1.3. Material Selection

It was established that the usual outgassing properties of known space-qualified materials – the Total Mass Loss (TML) and the Collected Volatile Condensable Materials (CVCM) values – were not adequate to determine whether outgassing of organic material was sufficiently low to be acceptable. A contamination study was carried out to simulate the deposition of organic material and its polymerisation under vacuum and UV radiation. In addition, outgassing investigations of materials and components were conducted with gas-chromatography/mass-spectrometry (GC/MS) analysis to determine the outgassing of organic species as a function of temperature and time. The species were enclosed in a glass vial that allows the specimen to be heated in an oven and purged by clean gas over extended periods of time, while occasionally gas samples were drawn for GC/MS analysis. This procedure was particularly useful as it revealed either the rejection or the acceptance of the component. The specimens were heated to the highest temperature compatible with their specifications and the duration was extended until acceptance was achieved, usually when the outgassing of organic molecules was near the detection limit. Since this method is more sensitive than residual-gas analysis under high vacuum, the bake-out procedure was designed in a similar way.

2.1.4. Cleaning and Bake-out

Generally, all hardware used for assembly was precision-cleaned before entering the clean-room facilities. The cleaning procedures included, with only a few exceptions, an ultrasonic bath with detergent and ultra-clean water. Solvent-compatible items were also cleaned with isopropyl alcohol and acetone. A special procedure was applied to cables before production of harnesses with methyl–ethyl ketone (now replaced by a special detergent) to remove possible residues of silicons inside the cable insulation. After wet cleaning, items selected for integration were subjected to a bake-out procedure and transferred to the clean area in double bags. The bake-out oven consists of a chamber with a controlled heating system and vacuum port for pump-out. All items were baked at the highest temperature compatible with the material of construction. Subassemblies were either baked at component level before assembly or, if subjected to an outgassing test as described above, baked at the temperature and duration determined by the test. This bake-out procedure replaced the usual space conditioning under high vacuum with heating and collecting contaminants at cold plates.

To guarantee the cleanliness of the six motor-driven mechanisms on SUMER, only dry lubrication of bearings with sputtered molybdenum disulphide (MoS_2) was considered acceptable. The motor coils were baked in an oven under clean gas purging (N_2 grade 5.0) at 200 °C for 48 hours before assembly of the component.

2.1.5. Ground Calibration

The responsivity of SUMER was characterized in the laboratory with a transfer source standard-calibrated by the Physikalisch-Technische Bundesanstalt (PTB) at the *Berlin Electron Storage Ring for Synchrotron Radiation* (BESSY II: Hollandt *et al.*, 1996). The transfer source is based on a hollow cathode (HC) discharge source, operated with inert gases to deliver a number of spectral lines inside the SUMER spectral range. However, the range could not be covered continuously, which left some gaps in the calibrated wavelength range (Schühle *et al.*, 1994). Recently, the PTB has opened an electron storage ring, the *Metrology Light Source* (MLS: Klein *et al.*, 2008 and Gottwald *et al.*, 2010), which operates with a continuous spectrum and with capabilities to calibrate space instruments.
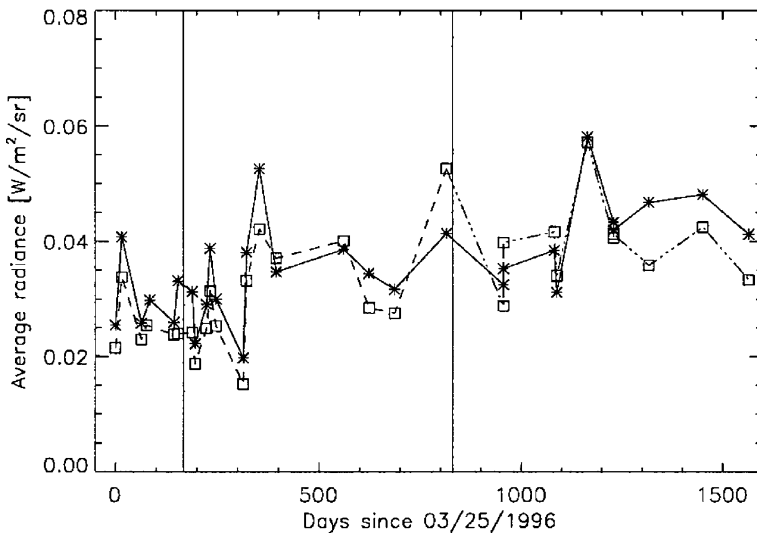
Figure 1 Common observations of the Mg X spectral-line emission at 62.4 nm in quiet-Sun areas by CDS (asterisks) and SUMER (squares) during the first years of SOHO operations (Pauluhn *et al.*, 2001).

2.1.6. Onboard Calibration Tracking

It is very important to track any degradation during the time of the mission. For SUMER it was possible to repeatedly observe UV-bright stars that come into the field of view (FOV) every year (Lemaire, 2002). Another way of tracking is observing the radiance of quiet-Sun areas that are unaffected by active regions with strong variability. The radiance of these quiet-Sun areas has been shown to vary only slowly over time periods of a solar-activity cycle (Schühle *et al.*, 1998). By observing the same objects simultaneously in common wavelength ranges, this method can be used for intercalibration between instruments. This has been done successfully over several years between UV instruments on SOHO (Pauluhn, Huber, and von Steiger, 2002). The *Coronal Diagnostic Spectrometer* (CDS) and SUMER spectrometers have made such common observations from the start of their operational phases. Figure 1 (taken from Pauluhn *et al.*, 2001) clearly depicts that by common observation of the quiet Sun, the degradation of the two instruments can be well accounted for, such that the remaining variation of the signal is not a systematic error of the instrumental throughput. This common intercalibration procedure, however, does not take into account longer-term effects on the CDS responsivity, which are discussed in the following section.

2.2. The Calibration of the CDS

The CDS is composed of a *normal incidence spectrometer* (NIS) and a *grazing incidence spectrometer* (GIS: Harrison *et al.*, 1995). The two instruments share a Wolter–Schwarzschild type II grazing-incidence telescope, a scan mirror, and a set of different slits. There is no entrance filter. The GIS uses a spherical grating that disperses the incident light into four spiral anode (SPAN) microchannel plate (MCP) detectors.

The NIS is composed of two stigmatic toroidal gratings that disperse the radiation into two wavebands (NIS 1: 30.8–37.9 nm and NIS 2: 51.3–63.3 nm). The NIS detector comprises an MCP Philips model G12-33 with pores of 12 μm diameter. The EUV photons are

converted into electrons via the photoelectric effect on the front face of the MCP, and are then amplified at about 756 V. The electron cloud is proximity-focused onto a P-20 phosphor coated on a fiber-optic output window. The visible phosphorescence is focused via a lens onto a Tektronix 1024 × 1024 charge-coupled device (CCD) with square pixels of 21 μm. The CCD is running cold, at a nominal temperature of − 70 °C.

2.2.1. Calibration

About two years before launch, the CDS instrument was calibrated end-to-end at the Rutherford Appleton Laboratory (RAL) against a "transfer" source that was absolutely calibrated using synchrotron emission. Details can be found in Lang *et al.* (2000). Immediately after launch, it became obvious that considerable departures (factors of two to three) from the pre-launch calibration were present. On 15 May 1997, a National Aeronautics and Space Administration (NASA)/Laboratory for Atmospheric and Space Physics (LASP) rocket carried an *EUV Grating Spectrograph* (EGS) that had been calibrated against synchrotron emission. On the same day, NIS measurements were performed and compared to the EGS ones (Brekke *et al.*, 2000), providing one key element in the long history of the in-flight calibration; see Del Zanna *et al.* (2010) for a summary. Further information on the NIS 1 was obtained with the *Solar EUV Rocket Telescope and Spectrograph* (SERTS)-97 rocket flight (Del Zanna *et al.*, 2001). The only in-flight radiometric calibration of all nine CDS channels (three second-order) was obtained by Del Zanna *et al.* (2001) with the line-ratio technique. The various NIS first-order calibrations were consistent, within 30 % to 50 %, with the SUMER calibration, as discussed during two ISSI workshops (Lang *et al.*, 2002), and as summarized in the previous section. Additional EGS rocket flights were flown in 2002, 2003, and 2004, but were not useful for the CDS calibration. An update to the CDS radiometric calibration was instead made possible by two *Extreme-Ultraviolet Normal-Incidence Spectrograph* (EUNIS) rocket-flights that took place in 2006 and 2007 (Wang *et al.*, 2011).

2.2.2. Detector Degradation and Long-Term Aging

MCPs are known to suffer a drop in gain owing to the exposure to solar radiation. For the NIS, this results in a depression at the core of the lines caused by exposures with the two-arcsec or four-arcsec slits (the so-called "burn-in" of the lines). This effect can be corrected for by looking at the burn-in in 90-arcsec slit exposures of the quiet-Sun (Thompson, 2000).

Figure 2 shows such a burn-in effect in a 13-year-long series of near simultaneous spectra taken with the narrow two-arcsec and the wide 90-arcsec slits.

It was thought that exposing with the 90-arcsec slit would significantly reduce (by more than a factor of three over 13 years) the responsivity at the wavelengths where the stronger lines in the spectra are present (Thompson, 2000, 2006). However, as shown in a series of articles (see references in Del Zanna *et al.*, 2010), this assumption turned out to be incorrect, because an overall decrease across all wavelengths of about a factor of two in 13 years was measured. Some wavelength-dependent effects turned out to be minor.

The overall decrease and its magnitude over more than 13 years of monitoring are readily apparent in the spectra shown in Figure 2. Note in the top panel of Figure 2 the discontinuity due to the temporary loss of contact with SOHO that occurred in June through September 1998. The resulting exposure to rather extreme and uncontrolled environmental conditions during that time interval caused significant changes in the characteristics of CDS, as of most other SOHO instruments. Figure 3 illustrates this effect on the NIS sensitivities and shows the measured aging in various wavelengths of the NIS 2 channel from 1996 to September
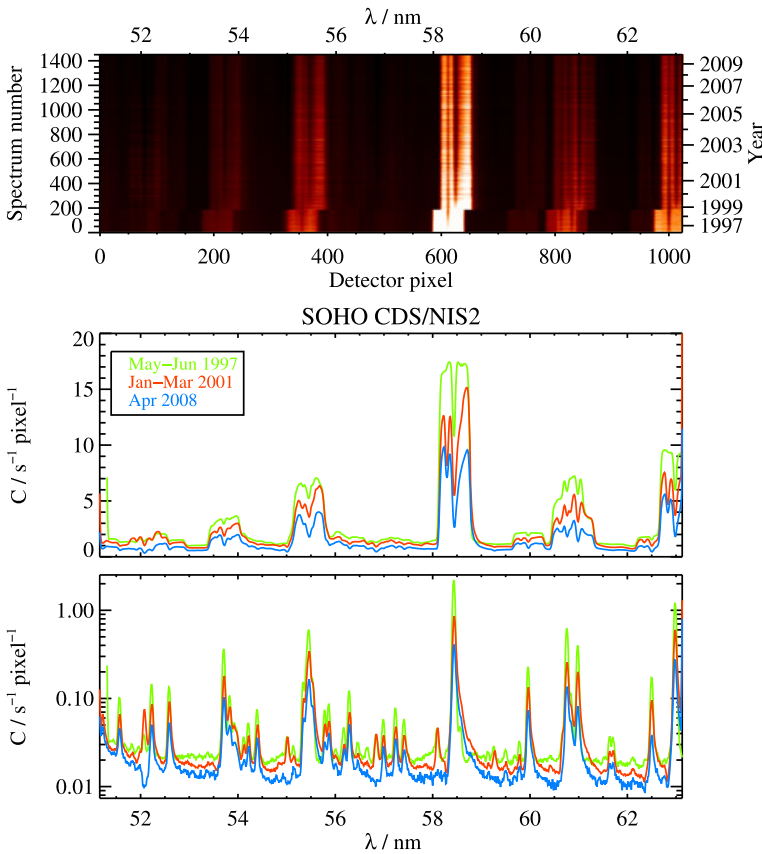
Figure 2 Top: the 13 years of CDS 90 arcsec NIS 2 data over the quiet Sun; the last spectrum shown here was taken on 7 April 2009. Middle: A sample of averaged 90-arcsec spectra at three different epochs. Bottom: The corresponding two-arcsec spectra. Notice the overall decrease in the count rates [C] in the two-arcsec and 90-arcsec spectra, and the marked decrease of count rates corresponding to the core of strong lines such as the He I 58.4 nm line. Figure adapted from Del Zanna *et al.* (2010).

2010. The coefficients of the fits to these data have been adopted as the default long-term radiometric correction in the latest version of the CDS analysis software. Figure 3 is similar to Figure 4 of Del Zanna *et al.* (2010), but shows data processed after the publication of that article, until September 2010. The curves shown in Figure 3 therefore reflect the most up-to-date estimates of the long-term variation of the CDS/NIS sensitivity, as currently included in the CDS analysis software.

The characterization of the long-term aging was found by Del Zanna *et al.* (2010) assuming that the quiet-Sun radiances in low-temperature lines are constant over time. Some support for this assumption comes from ground-based measurements of equivalent widths of photospheric and chromospheric lines (*e.g.* Ca II) over the quiet Sun (often Sun-center), which have provided firm evidence that the basal photospheric–chromospheric emission has not changed over the past three solar cycles (Livingston *et al.*, 2007, 2010).

The validity of this assumption has been confirmed by the overall agreement found between the CDS and the *Solar Dynamics Observatory/EUV Variability Experiment* (SDO/EVE) 2008 prototype irradiances (Del Zanna *et al.*, 2010) and by a direct CDS-
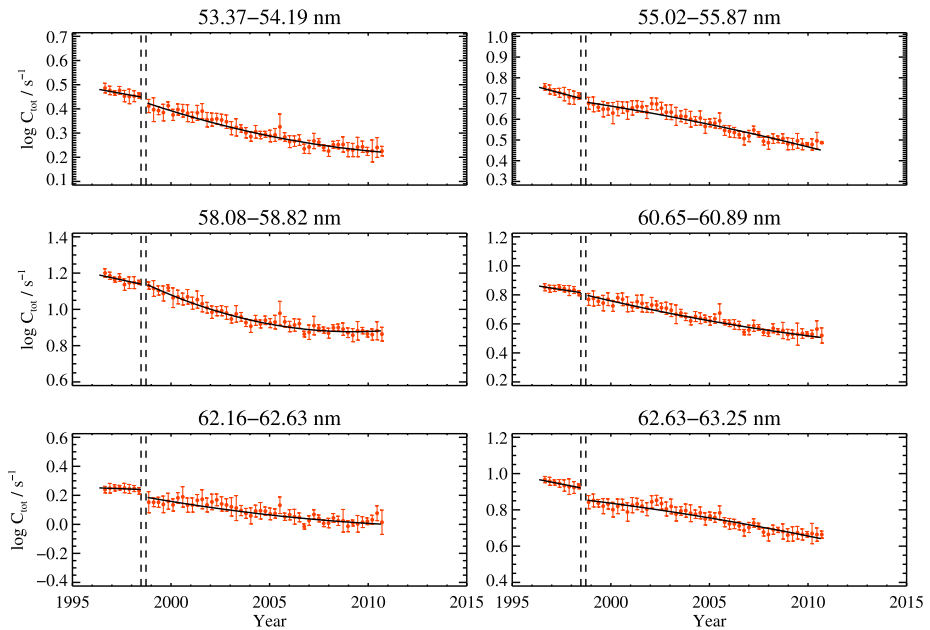
Figure 3 Time-dependence of average radiances in various wavelengths from CDS 90-arcsec quiet-Sun observations in the NIS-2 channel. Line radiances from individual spectra were grouped in bins of 90 days, obtaining an estimate of the mean and standard deviation in each time bin (points and bars). Black curves represent fits to these data. The two vertical dashed lines represent the times of loss (25 June 1998) and recovery (25 September 1998) of contact with SOHO.

EUNIS rocket-flight comparison of radiances (Wang *et al.*, 2011). This assumption does not necessarily contradict reports of an intrinsic variation of the solar source (see Section 2.1.6), whose magnitude typically is much lower than the extent of the long-term instrumental degradation and might be affected by the increase in solar activity in the 1996 − 2001 period considered by those studies (*e.g.* by Pauluhn and Solanki, 2003).

Del Zanna and Andretta (2011) proposed a new calibration for the He II line, which provided CDS irradiances in excellent agreement with those measured by the SDO/EVE prototype and by EUNIS (Wang *et al.*, 2011). As described by Kuin and Del Zanna (2007), there were gain-depression effects that lowered the spectral resolution in the strongest GIS lines. However, overall no signs of a decrease in responsivity were observed over a time period of ten years. This suggests that the grazing-incidence optics (telescope, common to the NIS) and the GIS grating have not suffered any contamination. It is therefore likely that the slow decrease in responsivity experienced by NIS is due to an overall decrease in the reflectivity of the normal-incidence gratings or to a lower sensitivity of the detector, either in the CCD or in the phosphorous coating on the anode in front of the MCP.

2.3. In-Flight Evolution of EIT

The *Extreme Ultraviolet Imager* (EIT) onboard SOHO is a Ritchey–Chretien telescope observing the Sun in four passbands of the EUV spectrum: 17.1 nm (Fe IX/X), 19.5 nm (Fe XII), 28.4 nm (Fe XV), and 30.4 nm (He II, Si XI). Four different multilayer coatings on the primary and secondary mirrors are used to select the passbands. A sector wheel at the front of
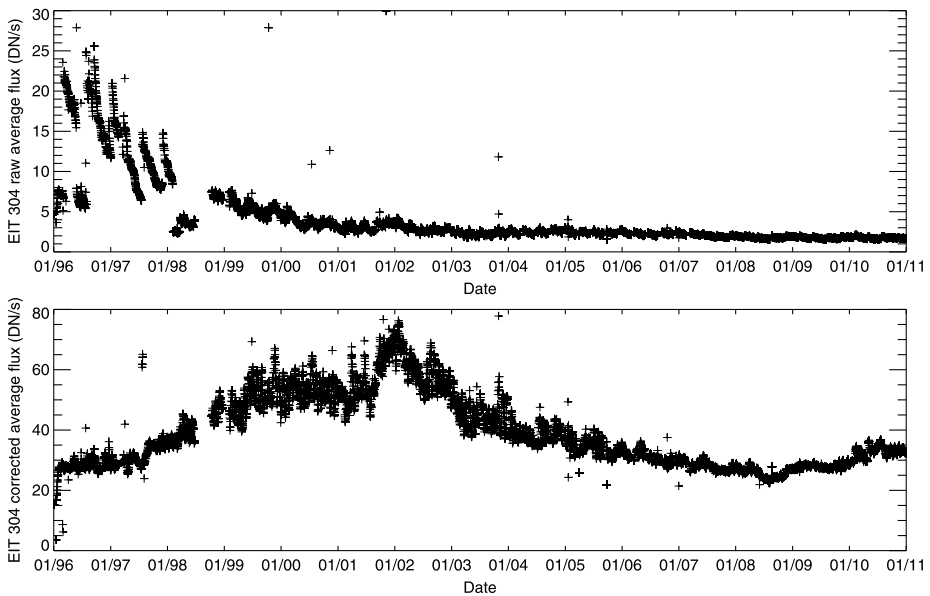
Figure 4 Average flux in the He II 30.4 nm band of EIT as a function of time before (top) and after (bottom) correcting for the degradation.

the instrument is used to select one of the four quadrants. Thin-film aluminum (Al) filters at the entrance of the instrument suppress the incoming visible and infrared (IR) radiation. Additional filters at the focal plane and on a filter wheel provide redundancy. The 1024 × 1024 CCD detector is passively cooled to about −70 °C. A shutter is used to time the exposures. A detailed description of the instrument can be found in Delaboudinière *et al.* (1995). Since its first light in January 1996, EIT has provided revolutionary views of the EUV Sun (Moses *et al.*, 1997). Its observations have been affected by serious degradation problems, but the degradation process could be understood and corrected for. A detailed analysis of the in-flight performances of EIT is given by Defise (1999).

2.3.1. Detector Degradation and In-Flight Correction

The total flux in EIT images rapidly showed strong variations that were obviously uncorrelated with the solar activity, as shown in Figure 4.

We see an initial rise of the signal followed by a steep decrease and periodic discontinuities. The initial rise is attributed to rapid outgassing of the instrument following the opening of its sealed door. There are two causes for the subsequent decrease: absorption by a contaminant on the detector surface, and radiation-induced degradation of its charge collection efficiency (CCE). For operational reasons, the partial pressure in the vacuum vessel was not low enough at launch so that immediately after launch, water condensed on the rapidly cooling detector. Modeling showed that the observed absorption could be explained by a thin layer of water, which is consistent with insufficient pumping at launch (Defise, 1999). Other contaminating compounds might be present as well, of course, but we have no way of identifying them in-flight, while water is known to be present in the residual atmosphere present in the vacuum vessel at launch. For stray-light protection, the CCD is isolated from
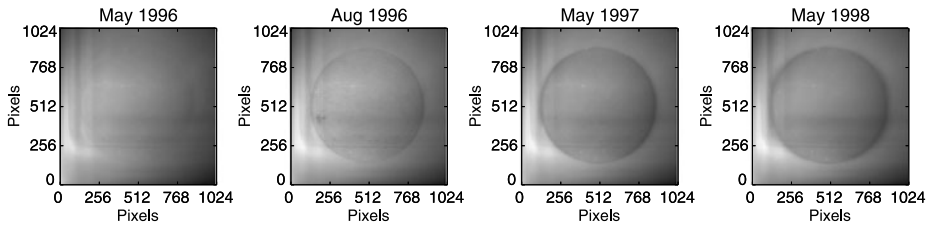
Figure 5 Evolution of EIT's calibration lamp images during the first two years of the SOHO mission (from Defise, 1999).
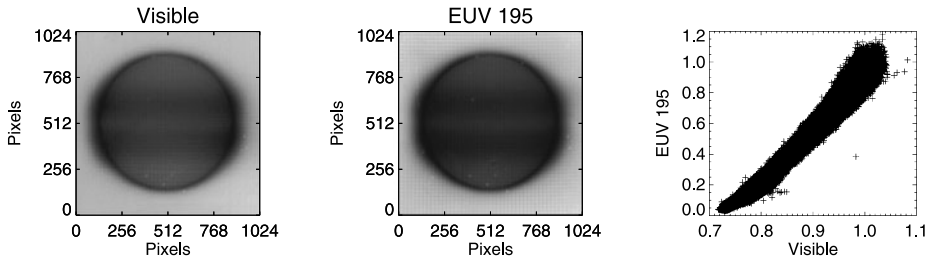

Figure 6 Left: white-light flat field for 8 February 2001. Middle: corresponding EUV flat field deduced from an offpoint of SOHO. Right: scatter plot of EUV *vs.* visible.

the rest of the telescope by a flange, and the only outgassing path to space are two labyrinths of low conductance.

The detector was regularly baked out to evaporate the water, but because of the low conductance to the outside, most of the water simply condensed on the walls of the back end and went back to the CCD when it was cooled again. This cycle is one cause for the oscillating response seen in Figure 4. The second component of detector degradation is illustrated in Figure 5. The four images show the evolution of calibration lamps (a light bulb illuminating the focal plane with visible light). We see the progressive imprinting of a negative average image of the EUV Sun, with the limb brightening and active-region bands clearly visible in the last image.

This is due to loss in the CCE of the detector. EUV light creates positive charges at the interface between the silicon (Si) and the silicon oxide (SiO_2) layer that thicken the dead layer. As consequence, in the regions that are on average the most illuminated, the CCE is decreased. By baking out the CCD regularly to about 20 °C, the dead layer is thinned and homogenized, thus restoring part of the original sensitivity (Defise *et al.*, 1997). These detector degradation effects have been understood and empirically modeled using calibration-lamp images. However, the images of Figure 5 cannot be used directly to correct the data, first, because they are white-light images, and second, because the light source does not illuminate the detector uniformly. The ratio between a calibration-lamp image and an initial-lamp image taken before the first light with a pristine detector has to be used. This gives a visible-light flat field, which can then be converted into an EUV flat field if one knows the relationship between visible and EUV degradation. To derive this relationship we used several off-point maneuvers of the SOHO spacecraft.

The set of displaced images taken during the maneuvers was processed using the algorithm of Kuhn and Loranz (1991) to separate the solar image from the flat-field features. Figure 6 shows the white-light flat field derived from calibration lamps for the date of the 8
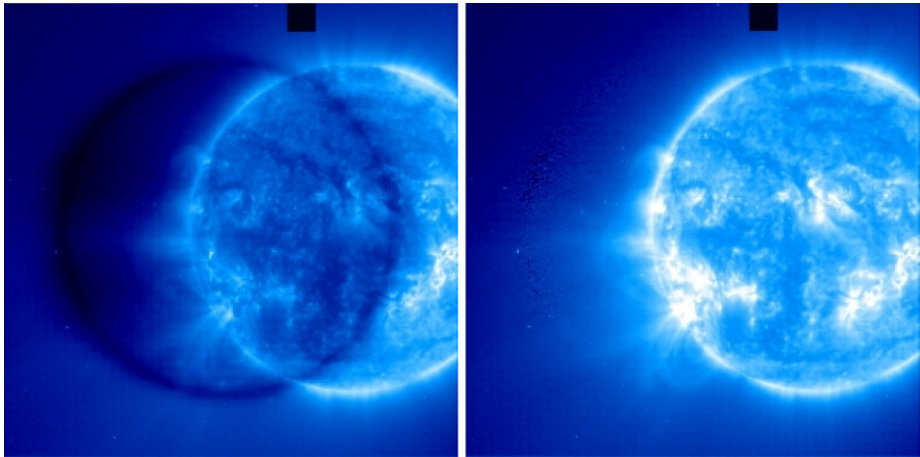
Figure 7 EIT 17.1 nm images taken during an off-point manoeuvre before and after correction.

February 2001 off-point (left), the EUV flat field (center), and the relationship between the two (right). A fit to this relationship (see Figure 8.7 of Clette *et al.*, 2002) is used to convert white-light calibration-lamp images taken regularly (about every two weeks) into EUV flat fields used to correct the images (see Figure 7). Calibration lamps have proven to be essential for calibrating the EIT instrument. The key to their successful use is the acquisition of a good reference image before first light.

Applying this to all images, we obtain a corrected EUV times series. The instrumental effects are taken out, revealing the solar variability. However, the corresponding time series of integrated fluxes still exhibit semi-periodic fluctuations, which indicates that not the entire degradation is accounted for by this procedure. Indeed, since the contaminant (whether only water or a mix of several compounds) is very thin, it is practically transparent to visible light and is therefore not revealed by the calibration-lamp images. The onboard flat-fielding thus corrects only for the CCE degradation, which is the dominant effect in the EIT response, however.

By comparing EIT and the *Solar EUV Monitor* (SEM) data, we concluded that the contaminant (probably essentially trapped on the cold detector) represents about 20 % of the total degradation (Clette *et al.*, 2002). To remove this remaining variation, we tied the EIT fluxes to the Mg II center-to-wing ratio index. For each period between two successive bake-outs, the CCE-corrected EIT integrated fluxes were correlated with the Mg II index and de-trended using a linear fit. Details about the procedure are given by Clette *et al.* (2002). We emphasize that this does not force the EIT fluxes to match a solar index; it only forces a linear relationship between the two, and the correction is 20 % at most.

Hock and Eparvier (2008) used the *Thermosphere Ionosphere Mesosphere Energetics* (TIMED)/*Solar EUV Experiment* (SEE) spectral-irradiance measurements instead of the Mg II index to correct for the variations remaining after CCE correction. They argued that TIMED/SEE observations would be better suited because Mg II is not sensitive to coronal temperatures. However, the authors showed that the Mg II-corrected EIT fluxes agree with the TIMED/SEE measurements within the uncertainties of the two instruments. Furthermore, this index has the advantage of being available continuously for the entire SOHO lifetime and of being determined independently from several sources.
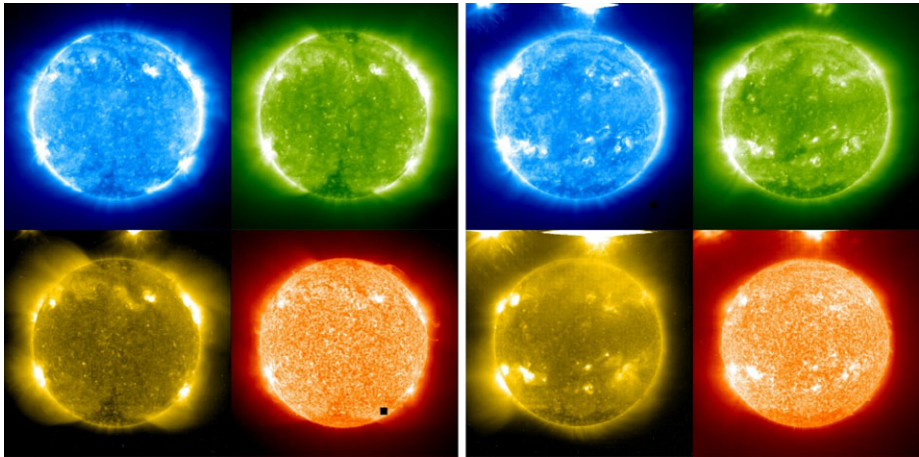
Figure 8 Visible-light leaks in EIT images. Left: after launch. Right: after the micrometeorite event of February 1998.

2.3.2. Filter Degradation

The Al filters at the front of the instrument and at the focal plane did not survive the launch, even though the telescope was launched under vacuum to avoid acoustic vibrations. Tears developed, which produced light leaks that were fortunately localized at the edges of the detector so that they did not significantly affect the image quality (Figure 8, left). However, in February 1998, after two years in orbit, the light leaks suddenly (from one image to the next) became much larger and the images were swamped by white light (Figure 8, right). The most probable explanation for this is a micrometeorite hit that produced a large pinhole in the front filters. Large amounts of white light could thus reach the focal plane, and reach the detector through the pinholes that formed in the back filter during launch. The solution to this problem was to insert one of the extra Al filters held by the filter wheel in the beam. Without this mechanism, EIT images would be almost unusable after 1998. This lesson should be remembered for future long-duration missions. Not only can the launch be harmful to these filters, but sudden degradation can occur at any time, especially if the spacecraft encounters harsh environments. In this case, the redundancy provided by a mechanism is essential.

2.3.3. Conclusion

Sixteen years of EIT observations have given us many examples of the problems that can be encountered during the lifetime of an EUV telescope. EIT shows no significant changes in its spectral selectivity, but variability of the detector sensitivity was a major hurdle. Part of this problem (the contamination by water) could have been avoided if the pressure in the vacuum vessel had been maintained at a low enough level up to the launch. This illustrates the importance of maintaining cleanliness during the whole lifetime of the instrument. The contaminants were also trapped in the back end of the telescope due to insufficient conductivity to the telescope section and to space. This problem was solved on the *Solar TErrestrial RElations Observatory/Extreme UltraViolet Imager* (STEREO/EUVI) by adding vents close to the detector. This practice should be maintained for future telescopes. Compared with other instruments such as the CDS or SEM onboard SOHO, we conclude that most of the variability of the instrument response (70 %) is explained by the degradation of the detector.
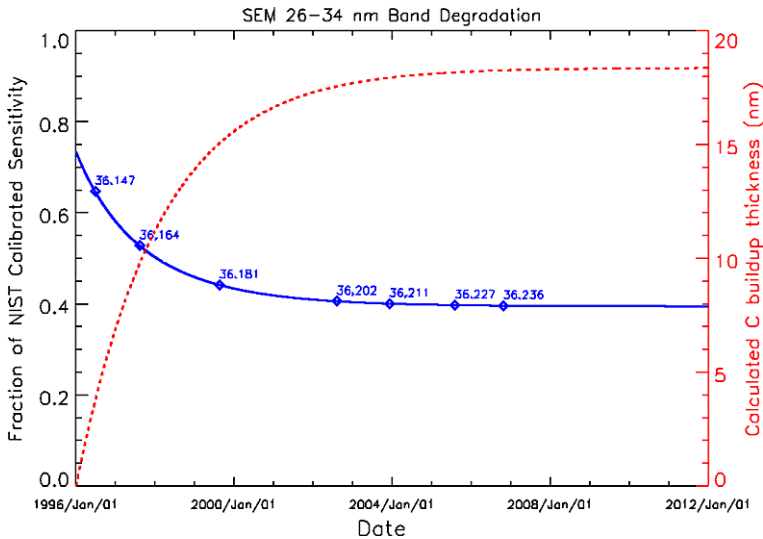
Figure 9 Degradation of the SOHO/CELIAS-SEM 26 – 34 nm band (blue, solid line) as measured by sounding-rocket underflights of a NIST-calibrated copy of the SEM (diamonds). The degradation is modeled as the build-up of a layer of carbon (red, dotted line). This is an updated version of the degradation trending first presented by McMullin *et al.* (2002).

This behavior is different from that of SEM, even though the two instruments observe in comparable wavelength bands. The degradation observed in SEM is explained in terms of a carbon deposit on the front filter, while on EIT there is no evidence of variation in the EUV response of either the filters or the multilayer coatings. This difference may find its source in a combination of factors such as different designs, materials, contamination control plans, locations on the spacecraft, *etc*.

2.4. SOHO/CELIAS-SEM

The *Solar and Heliospheric Observatory/Charge, Element, and Isotope Analysis System – Solar EUV Monitor* (SOHO/CELIAS-SEM: Judge *et al.*, 1998) is a simple transmission-grating spectrophotometer using an entrance Al filter to restrict the bandpass incident on the grating, and defining the bandpass of the zero-order signal. Detectors in the first-order are positioned to measure the 26 – 34 nm region of the solar spectrum, including the He II emission at 30.4 nm.

The SEM showed steady degradation of the first-order signal over the first seven years of operation, and after that the degradation has remained almost constant, as shown in Figure 9. The degradation has been tracked by a series of sounding-rocket underflights with a copy of the SEM instrument that is calibrated at the National Institute of Standards and Technology (NIST) with the *Synchrotron Ultraviolet Radiation Facility* (SURF) before and after flight. This way, the calibration of the sounding rocket can be applied to the on-orbit SEM, and the degradation measured.

It is postulated that the degradation seen by SEM is due to the build-up of a contamination layer on the front filter of the instrument. As no spectral information is available, it has been assumed that the major element causing contamination is carbon. Hydrocarbons from spacecraft outgassing, fuel return, *etc.* can hit the front filter; a certain proportion will

"stick" and can become polymerized by the solar UV radiation. As this layer grows, the EUV signal is more strongly attenuated. Figure 9 shows the degradation as measured by the sounding-rocket underflights and the modeled thickness of carbon required to cause this level of attenuation in the 26 – 34 nm band.

### 2.5. Long-Term Exposure Correction of VIRGO/DIARAD

The *Differential Absolute Radiometer* (DIARAD: Dewitte, Crommelynck, and Joukoff, 2004) is one of the radiometers of the *Variability of solar IRradiance and Gravity Oscillations* (VIRGO: Fröhlich *et al.*, 1995) package on SOHO developed at the Royal Meteorological Institute of Belgium. VIRGO/DIARAD has measured the Total Solar Irradiance (TSI) since 1996. The instrument is a dual-channel, side-by-side, self-calibrating absolute radiometer. Each channel is composed of a detector assembly, a cylindrical black-painted cavity with its associated precision aperture, a baffling system, a limiting aperture, and a shutter. Both cavities are mounted on a common heat sink. The DIARAD working principle is based on the compensation of heat in one channel's cavity while its shutter opens and closes every three minutes (Dewitte, Crommelynck, and Joukoff, 2004). When the shutter of the measuring channel is open, part of the solar radiation is absorbed by the cavity. Its induced heat flux is measured by the detector. When the shutter closes, a servo system compensates for the deficit of radiative power by dissipating an equivalent electrical power. When measuring with one channel, the other channel is used as a reference and its shutter is kept closed. For a detailed description of the instrument, see Crommelynck (1982), Crommelynck and Dewitte (1999), and Mekaoui *et al.* (2010).

### 2.5.1. Degradation Monitoring Strategy

Because the instrument is symmetric, each channel can be used as an independent measuring device with its own electrical, thermal, geometrical, and optical characteristics. These characteristics are the main parameters in determining the absolute value of the TSI. This last topic is still a matter of debate (Mekaoui *et al.*, 2010; Fröhlich, 2012; Kopp, Harber, and Heuerman, 2011; Kopp and Lean, 2011; Fehlmann *et al.*, 2012). While each channel of DIARAD is electrically self-calibrating, assuring the stability of the measurements of the absolute TSI value, the thermo–optical properties are subject to degradation and changes due to the long-term exposure to solar radiation.

This type of degradation is monitored and corrected for by ground processing. To achieve this, the left channel has measured the TSI every three minutes since 1996. During these three minutes, the left shutter is open for only half of the time. As a consequence, the total induced aging effect from the start of the measurements in 1996 – assuming its unique dependence on the exposure time – is caused by around 8.5 years of cumulative exposure to solar radiation. The right channel is operated for only 45 minutes every month. It is exposed for half of the time to solar radiation. Its total exposure amounts to three days from the start of the mission. Figure 10 shows the daily mean TSI measurements from the left channel (in green) and the 30-minute average of the right-channel measurements (in black, the first 15 minutes are excluded because of a transient effect). In this figure, the right-channel measurements have been adjusted to the left-channel measurements at the beginning of the mission in 1996. In 2012, the difference between the two channel measurements is around $1.2 \, \text{W} \, \text{m}^{-2}$ because of the left-channel degradation.

Figure 10 Temporal variation of the TSI measurements from VIRGO/DIARAD. Green symbols: daily mean TSI measurements from the left channel; black curve: the 25-minutes average of the TSI measurements made each month with the right channel; red symbols: the daily mean aging-corrected TSI measurements.
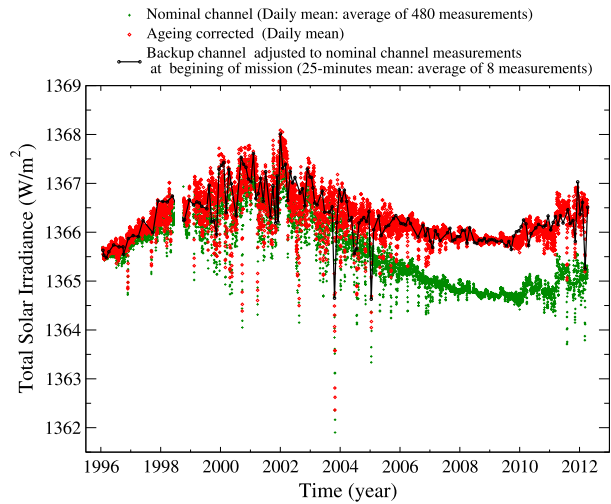
Figure 11 DIARAD-right minus DIARAD-left TSI measurements. The offset is removed at the beginning of the mission. The black curve is the computed aging correction from a variable nine-point running mean over the right – left difference.
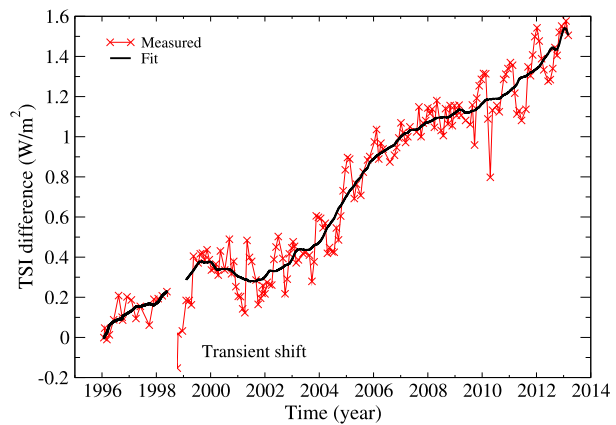
2.5.2. *Degradation Correction Implications*

The less-exposed channel gives valuable information on the long-term TSI evolution. Figure 10 shows the right channel, indicating that the difference between TSI minima in 2009 and 1996 is $0.15 \pm 0.17 \, \mathrm{W \, m^{-2}}$. This suggests that no significant increase is measured between the Solar Cycle 23 minima. Alternatively, these measurements can be used to correct the nominal (left-channel) for its aging.

For each monthly measurement with the right channel, left-channel measurements are made before and after. These measurements are then interpolated and compared with the right-channel measurements (simultaneous measurements with the right and the left channel are not possible). To reduce the uncertainty, it is important to compare the same means. Indeed, the right-channel measurement is a 25-minute average and so should the left-channel measurements be before interpolation. Figure 11 shows the difference between the right-channel measurements and the interpolated left-channel measurements. A fitted curve is used to smooth the difference. The values of this curve are then added to the left-channel measurements to take into account its degradation. This exposure-dependent aging is the

only correction applied by the team of the Royal Meteorological Institute who developed the instrument. Additional corrections are applied by the VIRGO PI-team. These exposure-independent corrections are based on the comparison with other radiometers (Fröhlich, 2003). These results are still a matter of debate and have yet to be reproduced on the ground.

## 3. Degradation of the Hinode/EIS Detectors after Five Years in Orbit

The *Hinode* satellite was launched in September 2006 and is still operational. *Hinode* is a Japanese satellite with payloads funded by JAXA–ISAS, NASA, ESA, and UKSA (previously STFC). *Hinode* is in a Sun-synchronous low-Earth orbit (altitude ≈ 600 km), which allows for continuous observing of the Sun. There are three solar telescopes onboard *Hinode*: the *Solar Optical Telescope* (SOT: Tsuneta *et al.*, 2008), the *X-Ray Telescope* (XRT: Golub *et al.*, 2007), and the *Extreme-UV Imaging Spectrometer* (EIS: Culhane *et al.*, 2007).

The *Extreme-UV Imaging Spectrometer* (EIS) has a large effective area in two EUV spectral bands; $17-21$ nm and $25-29$ nm. There are two CCDs, one for each wavelength range. The CCDs are e2v device type CCD 42-20, which have an array size of 2048×1024 pixels, a pixel size of $13.5\times13.5\,\mu m^2$, are thinned for back-illumination, and employ multi-pinned phase (MPP) technology in asymmetric inverting-mode operation (AIMO), which allows for low dark-current levels without excessive cooling (see Culhane *et al.*, 2007 for the EIS instrument article).

The in-orbit operating temperature range of the CCDs is ≈ -36 °C to -46 °C; the variation is due to the perihelion and aphelion of the orbit. The assembly and pre-launch calibration of EIS were performed at RAL (UK). The components of EIS (entrance filters, primary mirror, slit/slot mechanism, shutter, grating, and CCDs) are housed in a carbon-composite structure. Post-launch, a pixel shift of eight to nine pixels in the spectral direction was observed when compared with the pre-launch calibration. The shift was attributed to the thermal stabilization and out-gassing of the instrument, and a correction was made in the software to accommodate the shift. Regular calibration studies are run weekly, monthly, or quarterly, depending on the types of study, which include dark exposures, Light Emitting Diodes (LEDs) flat-fields, synoptic, quartz-crystal microbalance (QCM), and full CCD spectral scans.

3.1. Hot and Warm Pixels

The hot and warm pixels are defects in the CCDs, where the rates of charge leakage are higher because of defects in the Si. A few exist in the as-manufactured device, and radiation damage accumulated over time adds to these. In the EIS orbit, the radiation effects are dominated by passages through the South Atlantic Anomaly (SAA). The hot and warm pixels are seen as spikes in the data that need to be calibrated out, *e.g.* using eis_prep (an IDL routine available in the EIS Solarsoft distribution). The positions of the warm and hot pixels are mapped and the information provided to eis_prep. The distinction between hot and warm pixels is somewhat arbitrary. Pre-launch, hot pixels were defined as pixels where the room-temperature dark current rate 25 000 electron per pixel per second, for consistency with the criterion used by e2v in device screening and characterization. In orbit, it has been found that radiation damage also causes pixels with lower charge-generation rates, but which are still above the CCD noise level, and so have to be taken account of. These are termed warm pixels, and the criterion used is that the dark signal is $> 5\sigma$ above the mean for a 100-second dark exposure. The hot and warm pixels generally follow the usual exponential temperature
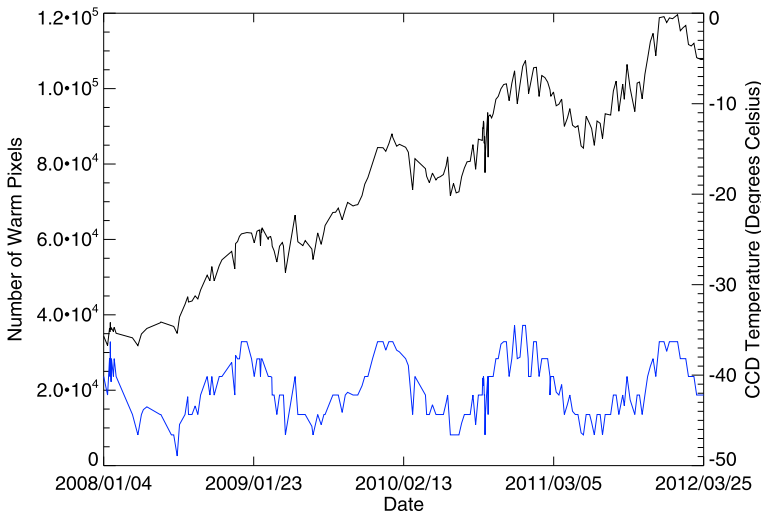
Figure 12 Number of warm pixels for the EIS CCDs. The (upper) black curve is the number of warm pixels and the (lower) blue curve is the corresponding CCD temperature.

dependence of dark current in silicon, which means that cooling is effective in reducing the impact on the data. For EIS, the CCD temperature is higher than the pre-launch prediction of below $-50\,°C$, so the hot and warm pixels are greater in number. The XRT instrument on *Hinode* has the same type of CCDs as EIS, but they operate at a much colder temperature ($\approx -80\,°C$) and therefore have no problem with warm pixels. The increase in hot pixels follows an approximately linear trend over time. As of April 2012, the number of hot pixels per each CCD quadrant was ≈ 7800, which is equivalent to 1.5 % of the imaging area. The rate of increase of the warm pixels changes significantly and is temperature dependent because of the dark-current variation with temperature (annual variations in the CCD temperature are due to aphelion and perihelion), as shown in Figure 12.

As of March 2012, the average number of warm pixels for each CCD quadrant was ≈ 108 thousand (which is ≈ 21 % of the imaging area). The warm pixels are currently in a decreasing phase (the CCD temperature is decreasing). The number of warm pixels in December of each year (hottest point) is increasing by ≈ 16 thousand per year. Based on this estimate, the number of warm pixels will be

- ≈ 136 thousand (26 % of the imaging area) in December 2012,
- ≈ 152 thousand (29 % of the imaging area) in December 2013.

When a 30 % warm pixel level is reached, the spectral-line-fit parameters will be affected (private communication, P. Young, 2012). When the number of warm pixels (per CCD quadrant) reaches 157 286, the 30 % level will have been reached. The highest number recorded so far was 120 312 on 5 January 2012 (on the short-wavelength CCD).

3.2. Flat Field and EIS Sensitivity

The sensitivity levels for the EIS CCDs are monitored by using the data from LED flat-field images. The LEDs are blue, $\lambda_{peak} \approx 430$ nm, which approximately matches the absorption depth for the EUV photons. The flat fields show that the intensity levels have not changed significantly since launch (Figure 13), which indicates that the CCDs are not contaminated.
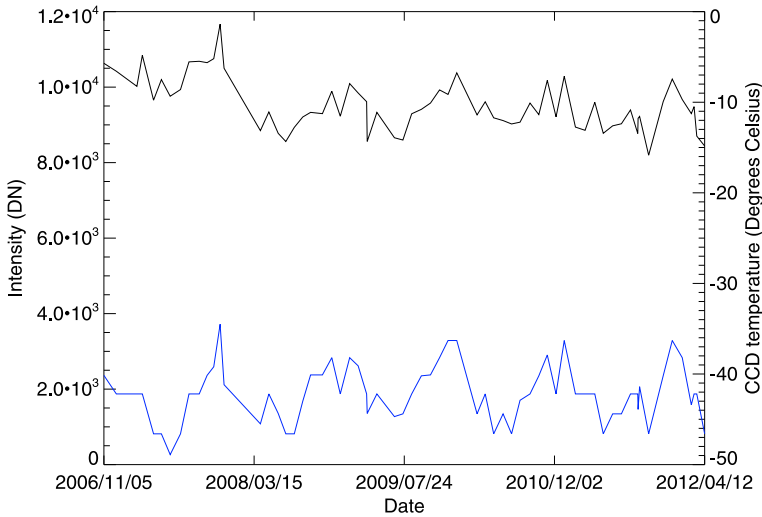
Figure 13 Flat-field intensity levels for the EIS CCDs using EIS LEDs (averaged over a 450×450 pixel area). The (upper) black curve is the intensity level and the (lower) blue curve is the corresponding CCD temperature.

Figure 14 EIS sensitivity rate using He II observations (courtesy J. Mariska, NRL).

He II 256.32 Å
$I_0 = 139$
$\tau_1 = 471$ days
const = 118
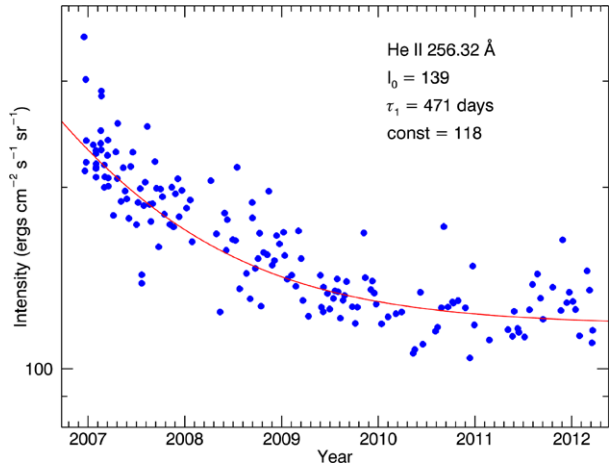
A synoptic observation of a patch of quiet-Sun is made every week. The record of He II observations shows that the EIS sensitivity decay rate is slowing (Figure 14).

The best-fit expression is now an exponential plus a constant. It is not clear yet whether some of the flattening is due to solar-cycle effects. Figures 13 and 14 indicate that the sensitivity decay is due to contamination/degradation of the optical elements rather than the CCDs. The sensitivity changes are factored into the EIS analysis software (eis_prep).

The QCM (located at the entrance aperture) readings for EIS have been taken at weekly intervals since launch and provide an indication of the contamination levels of the critical instrument surfaces. The QCM data have shown a slight increase from year to year, which is to be expected. The QCM data from 2010 to 2011 saw a lower increase than in previous

years. This agrees with the sensitivity measurements, which show that the decay rate is slowing (*i.e.* less contamination).

3.3. CCD Annealing

The plan so far has been to refrain from performing a CCD anneal or bake-out (heating the CCDs to around $+35$ °C) for as long as possible, as it presents a small risk to the instrument (heaters require a high-power mode). Discussions at the recent EIS team meeting (April 2012) concluded with an annealing estimated for December 2013, which will be after seven years in orbit. Initially it was planned to perform a bake-out when the optical performance degraded, but the flat-field intensity levels suggest that there is no contamination on the CCDs (Figure 13), and therefore a bake-out will not improve the optical performance. The current driver for an anneal is the number of warm pixels, and not contamination. The warm pixels will compromise the science when a 30 % level is reached. The warm pixels are also impacting the EIS data compression; the effect being that the EIS telemetry allocation is reached because estimates are wrong (data compression degradation). The data-compression factors for EIS have been reduced by 10 % (five years into the mission). Until now, this reduction is only for the *hot* season (October to April), when warm pixels are increasing. Data compression factors will be returned to nominal in the *cooler* season (April to October), when warm pixels are decreasing. It is hoped that following bake-out, the data-compression performance will revert to the post-launch level. The EIS operations team will have to experiment with anneal temperatures ($+35$ to $+45$ °C) and durations to maximize the recovery prospects of the hot and warm pixels.

3.4. Conclusion

The EIS instrument behavior is "nominal" for a Low-Earth Orbit (LEO) space mission of its age. The CCDs are sustaining radiation damage as expected, although the amount of dark current per damaged pixel is higher than originally predicted because of the higher operating temperature (planned to be around -60 °C, achieved at around -45 °C). The warm pixels will impact the science operations once their level reaches 30 % of the imaging area. At present, they are mapped and removed via the EIS processing software. It is hoped that a bake-out ($\approx +35$ °C) will recover most of the warm pixels. Bake-out is currently planned for the end of 2013. The data-compression performance was affected when the warm pixels reached a 25 % level (five years into the mission). EIS compression factors are now reduced by 10 % during the *hot* season. The optical performance degradation is better than expected (compared with similar missions and duration in orbit) – it is expected that 1/e will be reached in seven years.

4. Long-Term Stability of the Photometric Response of the STEREO/HI-1

The twin *Solar TErrestrial RElations Observatory* (STEREO) spacecraft, which were launched in October 2006, are in heliocentric orbits at approximately 1 AU, with each spacecraft separating from the Earth by 22.5° per year. STEREO-A is leading the Earth in its orbit, whilst STEREO-B is trailing the Earth.

The *Heliospheric Imager* (HI: Eyles *et al.*, 2009) instruments form part of the *Sun–Earth Connection Coronal and Heliospheric Investigation* (SECCHI: Howard *et al.*, 2008) suite of remote-sensing instruments onboard each of the STEREO spacecraft. They are primarily

Figure 15 Measured *versus* predicted intensities (in DN s^{-1}) for a large number of stars in the HI-1A (top) and HI-1B (bottom) initial photometric calibrations. Updated from Bewsher *et al.* (2010).
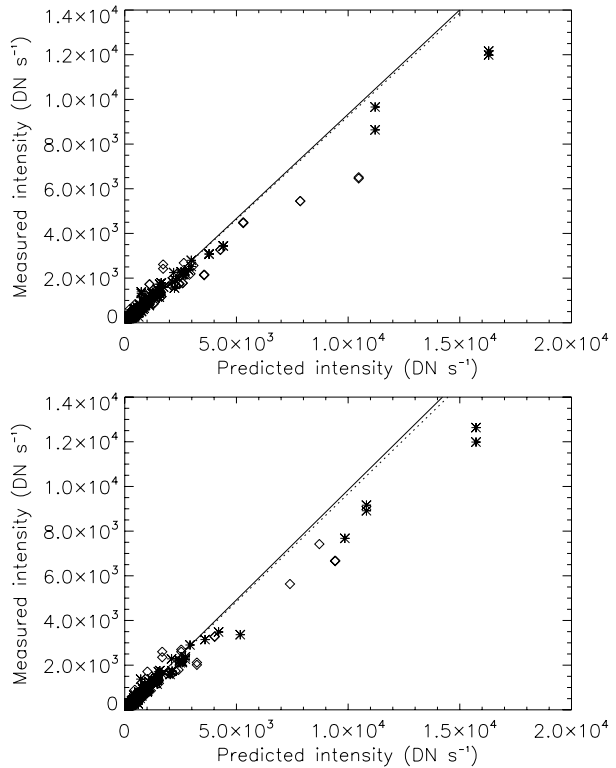
designed to observe coronal mass ejections (CMEs) as they propagate from the solar neighborhood to Earth-like distances and beyond. Each HI instrument consists of two visible-light cameras [HI-1 and HI-2] with field-of-view (FOV) diameters of 20° and 70°, respectively, whose optical axes are aligned with the ecliptic plane in orientations that provide an overall coverage of $4-88.7°$ solar elongation. The HI-1 and HI-2 telescopes consist of CCD cameras with fairly conventional transmission optics that are "buried" within complex baffle systems to provide the necessary high levels of solar stray-light rejection for imaging the faint emission from CMEs. The spectral band passes are $630-730$ nm and $400-1000$ nm for HI-1 and HI-2, respectively. The CCDs are passively cooled to below -70 °C.

4.1. Initial Photometric Calibration

The initial photometric calibration of the HI-1 telescopes (Bewsher *et al.*, 2010) was based on data from the start of STEREO mission operations up to December 2008. The intensities of stars with R magnitudes ≤ 12 and within 100 pixels radius from the center of the FOV were measured using aperture photometry. The stars and their spectral types were identified from the NOMAD catalog (Zacharias *et al.*, 2004). Predicted intensities were calculated by folding standard stellar spectra $S(\lambda)$ (Pickles, 1998) through an optimized model of the instrument-response function. The model of the instrument response was optimized using all available pre-flight calibration data, CCD and optics manufacturer response specifications, *etc.*

Table 2 The photometric calibration factor [μ] and the number of stars used to determine μ.

	Orbit 1	Orbit 2	Orbit 3	Orbit 4	Orbit 5	Overall
HI-1A	0.926	0.933	0.927	0.930	0.935	0.930
No. stars	430	418	433	424	428	2141
HI-1B	0.998	0.987	0.989	0.993	0.981	0.989
No. stars	387	384	455	417	368	2029

Figure 15 shows the measured *versus* predicted intensities for large populations of stars. Apart from a few outliers at high intensities (due to detector saturation effects), the stars lie close to a fitted straight line of the slope μ, *i.e.* $C_{\text{measured}} = \mu C_{\text{predicted}}$.

The photometric calibration factor [μ] represents an overall normalization error in the instrument response, the value $\mu = 1$ represents a perfect calibration. The values obtained for μ were 0.93 and 0.99 for HI-1A and B, respectively, with the total number of stars fitted being 903 and 541. No significant differences in μ were found according to spectral type, which confirms the validity of the instrument spectral response model.

4.2. Photometric Response Stability

To evaluate the photometric response stability, the above analysis was performed separately for each of the complete orbits of the STEREO spacecraft. The derived values for μ are shown in Table 2. The values for orbits $1-4$ (relative to the background star field) are taken from Bewsher, Brown, and Eyles (2012), and the values for orbit 5 and the overall value of μ were newly derived for this article. As previously, μ was determined using stars within 100 pixels radius from the center of the FOV (Bewsher, Brown, and Eyles, 2012). Complete orbits were used to avoid any possible systematic effects due to different star populations being used in each case.

It is clear from Table 2 that there are no systematic changes in the photometric response of either instrument at a level of 1 % or better. The analysis was also repeated for various selected regions of the FOV, and the response was again found to be stable to 1 % or better, although some variations at a level of $2-3$ % in the value of μ for different regions of the FOV were found, indicating some small systematic errors in the HI-1 flat-field corrections (Bewsher, Brown, and Eyles, 2012).

4.3. Conclusions

We have shown that from the start of mission science operations until the end of the fifth orbit of the two spacecraft relative to the background star field (5 December 2011 and 18 July 2012 for STEREO A and B, respectively), the photometric response of the HI-1 cameras has remained stable to 1 % or better. This is significantly better than the long-term stability of the white-light coronagraphs onboard the SOHO mission, where Thernisien *et al.* (2006) found a decrease of sensitivity of the *Large Angle and Spectrometric Coronagraph* (LASCO)-C3 instrument by 3.5 % over eight years of operation, whilst Llebaria, Lamy, and Danjurd (2006) reported a degradation of the LASCO-C2 instrument by 0.7 % per year. Whilst white-light instruments are not as sensitive to degradation as UV instruments, the excellent stability of the HI instruments vindicates the extensive precautions taken during their design and development.

5. SOLSPEC: A Spectrometer with Onboard Control of Aging

SOLar SPECtrum (SOLSPEC) is a spectrometer, that flew several times on the Space Shuttle, and its twin instrument was placed on the *European Retrievable Carrier* (EURECA) platform for ten months. The Shuttle flight has gathered data to build the *Atmospheric Laboratory for Applications and Science* (ATLAS) 1 and 3 spectra (Thuillier *et al.*, 2009), which comprised the *Upper Atmospheric Research Satellite* (UARS) / *Solar Ultraviolet Spectral Irradiance Monitor* (SUSIM) and *Solar Stellar Irradiance Comparison Experiment* (SOLSTICE) data from Lyman α (121.6 nm) to 200 nm, and ATLAS-*Shuttle Solar Backscatter Ultraviolet* (SSBUV), SUSIM, and SOLSPEC from 200 to 400 nm, ATLAS-SOLSPEC from 400 to 850 nm, and EURECA- *SOlar SPectrum* (SOSP) from 800 to 2400 nm. The ATLAS spectra are calibrated into the absolute radiometric scale of the black-body radiator of the Observatory of Heidelberg, NIST standards spectral irradiance (tungsten and deuterium lamps). The SOLSPEC instrument has been upgraded for operations onboard the *International Space Station* (ISS) by implementing several changes given the lessons learned from the previous missions and by adding several new components to provide an instrument able to operate for several years in the space environment. SOLSPEC has now been in operation onboard the ISS since February 2008. To cover the $165 - 3080$ nm range, three double spectrometers are used that are equipped with concave holographic gratings made by Jobin–Yvon. By rotating the six gratings mounted on the same mechanical axis, the range $165 - 3080$ nm is scanned in ten minutes with a mechanical precision corresponding to 0.01 to 0.1 nm, from the UV to the IR channels. To reduce the flat-field effect, diffusers are placed between the entrance pre-slit and spectrometer first slit. As the ISS environment could not always be clean in terms of contamination, and as the diffusers could degrade by EUV solar radiation, two wheels carrying a hole and two quartz plates each can be placed alternatively in front of the entrance pre-slit. These plates allow protection of the entrance slits from the deposition of contaminants, which can be ultimately polymerized by the solar EUV. In that case, the quartz-plate transmission decreases; however, it can be measured in-flight by using the ratio of solar observations with and without the quartz plate in front of the entrance slit. One plate is mainly used for each observation. Using the Sun, its transmission is compared with the infrequently used quartz-plate transmission. For each spectrometer, a wheel is equipped with second-order and/or neutral filters. The latter are used to reduce the signal given by the instrument responsivity and the solar-irradiance variation with wavelength.

5.1. Pre-Flight Absolute Calibration

SOLSPEC has been calibrated at the PTB using a black-body radiator. One of these black-body sources (BB3200pg) represents the primary standard for the realization of the spectral irradiance scale (Sperfeld *et al.*, 1998). Taking into account the distance between the black-body source and the SOLSPEC entrance slit, the size of the entrance slit, the black-body aperture, and the black-body temperature, the spectral irradiance is calculated for any given wavelength using the Planck law. The black-body cavity temperature is around 3000 K and it is known to within 0.44 K. Because the black-body emission is calculated and its ratio to the count number is recorded by SOLSPEC, one can convert the solar signal to absolute irradiance. Below 200 nm, the black-body source does not generate a strong enough signal, and hence deuterium (D_2) lamps provided by the PTB were used. During the calibration campaign, several spectra using the internal lamps were recorded as a reference in the relative scale. For the whole spectral range, the accuracy of SOLSPEC stays within 3 %. The SOLSPEC instrument is described in detail by Thuillier *et al.* (2009).

Figure 16 Transmission degradation of the quartz plate used for the UV–VIS solar spectrum measurements. The transmission is measured by comparing the signal with and without the quartz plate.
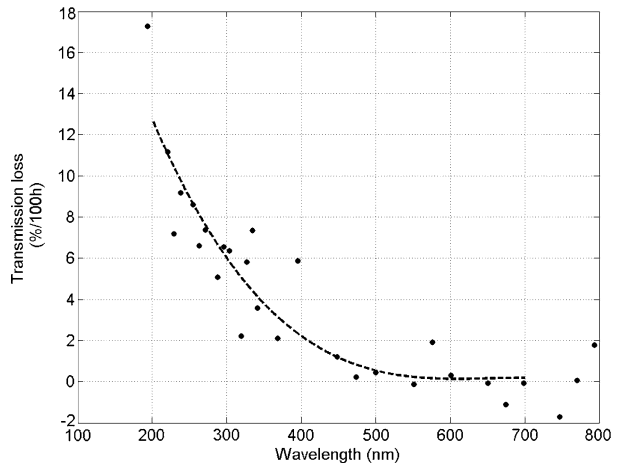
5.2. Onboard Calibration Means and Instrument Degradation in Space

D_2 and tungsten-ribbon lamps are used for checking the instrument stability with time. The light from these sources is carried by using optical fibres, mirrors, and lenses. The relationship between the mechanical position of the gratings and wavelength is measured by using a hollow-cathode (HC) lamp filled with argon (Ar), which delivers lines in the UV, visible, and near-IR. These lines also allow measuring the instrument slit function and the dispersion law (relationship between the grating position and wavelength).

Degradation in visible and IR domains is of about a few percent, and can be corrected for by measuring the transmission of the quartz plates and by using the internal ribbon tungsten lamps. As expected, the degradation in the UV is significant.

Figure 16 shows the transmission loss of the most frequently used quartz plate. The instrument responsivity change is derived from comparing the transmission of the second quartz plate (infrequently used), direct quartz-plate transmission measurements, and D_2 lamp data. After the D_2 lamp power-supply failure, we used the HC lamp lines, which are intensity-based, according to the following principle:

- In the laboratory as well as in orbit, we have verified that the lines emitted by the HC lamp have a covariance intensity change in time. In other words, the ratio of line intensity at two different wavelengths is constant, *i.e.* independent of the line intensity, which slowly decreases probably because of a gas leakage.
- Because the aging is corrected for (as explained above), the HC-lamp line intensity can be corrected for in the visible (or IR) spectrometer, and the percentage of the correction is in particular applied to the UV lines, which in turn provides data to correct the UV spectrometer responsivity.

5.3. Conclusion

The SOLSPEC design has been validated by the *SpaceLab I*, ATLAS 1, 2, and 3, and the EURECA missions. However, the duration of these missions were about one week except for EURECA, which lasted ten months. For a mission aiming to operate for several years, it was necessary to design an instrument with its own capability to provide data for aging corrections given its location in space.

6. Solar Instruments Onboard PROBA2

The *Project for On Board Autonomy* (PROBA) satellites are part of ESA's In orbit Technology Demonstration Programme, *i.e.* missions dedicated to the demonstration of innovative technologies through small satellites. On 2 November 2009, PROBA2 was launched into a Sun-synchronous polar orbit, which allows quasi-permanent solar observation. Two solar observation experiments, the *Sun Watcher with Active Pixels and Image Processing* (SWAP: Seaton *et al.*, 2012; Halain *et al.*, 2012) and the *Large-Yield RAdiometer* (LYRA: Hochedez *et al.*, 2006) on PROBA2 are test platforms for new technologies.

The absolute radiometric response of the two instruments, through collaboration between the Max-Planck-Institut für Sonnensystemforschung (MPS) and the PTB, has been established before flight at the primary radiometric source standard: the synchrotron radiation beamline of PTB at the *Berlin Storage Ring for Synchrotron Radiation II* (BESSY II).

6.1. Characterization of SWAP Degradation

SWAP is a single-band EUV telescope that observes the solar corona in a passband centered on 17.4 nm and with a 54×54 arcmin FOV, and has a novel off-axis Ritchey–Chretien design with two mirrors with multilayer coatings for EUV reflectivity and a complementary metal-oxide-semiconductor (CMOS) active pixel sensor (APS). A scintillator coating (P43) converts EUV photons into visible photons to which the detector is sensitive. Spectral selection is achieved by the combination of multilayer coatings and two Al-foil filters, one of which is located at the entrance aperture and the other in front of the focal-plane assembly. SWAP has operated essentially continuously since shortly after PROBA2's injection into its polar Sun-synchronous orbit in November 2009 at an approximate altitude of 725 km. Additionally, since SWAP does not have a door or shutter, its optical and electronic systems are continuously exposed to EUV input from the corona. We characterize SWAP's degradation in three ways: first, we compare the total response of the instrument to well-calibrated spectral measurements from the *Extreme Ultraviolet Variability Experiment* (EVE: Woods *et al.*, 2012; Didkovsky *et al.*, 2012) onboard the *Solar Dynamics Observatory* (SDO) spacecraft; second, we measure the number of improperly performing pixels in SWAP's 1024×1024 pixel CMOS detector; and finally, we roughly measure the evolution of SWAP's flat-field using a set of onboard LEDs. More detailed information on the ground-based calibration from PTB/BESSY II is discussed by Seaton *et al.* (2012), and the in-flight calibration by Halain *et al.* (2012).

6.1.1. Spectral Response

Since it is not possible to obtain in-orbit EUV images of a standard and well-calibrated source, degradation in the SWAP response function must be measured indirectly. To do this, we compared the mean SWAP response per pixel for solar images obtained regularly throughout the mission to corresponding spectra from EVE. To achieve this comparison, EVE spectra were first converted from units of total flux per wavelength to photon flux, then modulated by the laboratory-measured SWAP response function, and integrated across SWAP's entire bandpass. This procedure yields a single value with units of $\mathrm{DN\,s^{-1}\,pixel^{-1}}$ that we compared to the mean instrumental response in images obtained at the same time as the corresponding spectrum.

We then compared the evolution of these two values over time to assess the rate of degradation of SWAP's overall response over the course of the mission. A multiplicative factor
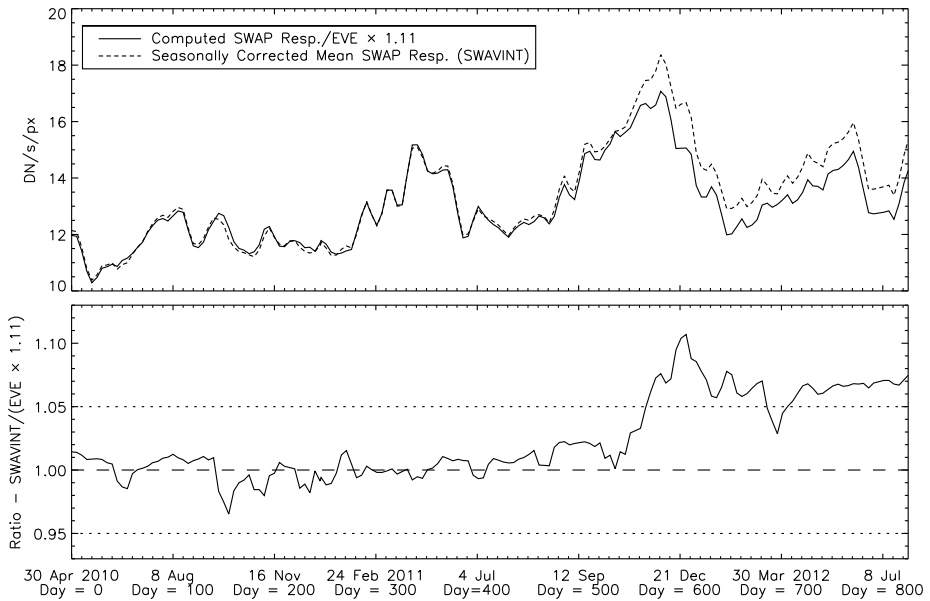
Figure 17 Comparison of SWAP measured intensity (blue-dashed) and SDO/EVE computed intensity (black-solid). The top panel shows the variation of intensity with time due to changes in solar irradiance near 17.4 nm, the lower panel shows the ratio of the two values over time. Adapted from Halain *et al.* (2012).

of 1.11 was applied to the EVE-based curve before our analysis. The need for this factor is probably the result of a combination of uncorrected degradation of EVE in orbit and error in measuring the SWAP response in the laboratory; the factor to be used was measured empirically and might be the result of many different contributions. Figure 17 shows this comparison; although the two curves are closely correlated, driven by the variation in coronal irradiance near 17.4 nm, they diverge at the end of 2011, the reason for which is still unclear.

6.1.2. Detector Degradation

A potentially more significant problem for SWAP is the breakdown of electronic components, especially those associated with its CMOS–APS detector, which is the first of its kind used for an EUV solar telescope. A complete discussion of SWAP's detector and its on-ground performance testing was given by De Groof *et al.* (2008). Unlike CCD detectors, which have been used in nearly all solar-imaging missions for decades, each pixel in a CMOS–APS detector has its own analog (amplifier) readout electronics, so a failure of these electronics can render only individual pixels inoperable. We monitored the detector performance primarily by tracking the number of hot pixels removed by the de-spiking routine in SWAP's image-calibration software. This value is strongly influenced by the evolution of detector temperature, therefore to separate changes in detector performance from the thermal evolution of SWAP, we modeled the temperature dependence of hot pixels using an empirically determined polynomial model and normalized the evolution of spikes in time using this model. Figure 18 shows both the normalized and non-normalized curves for a period of about 700 days after the end of PROBA2's commissioning period. In the normalized plot, the number of spikes clearly increases linearly in time at a rate of about 13 spikes per
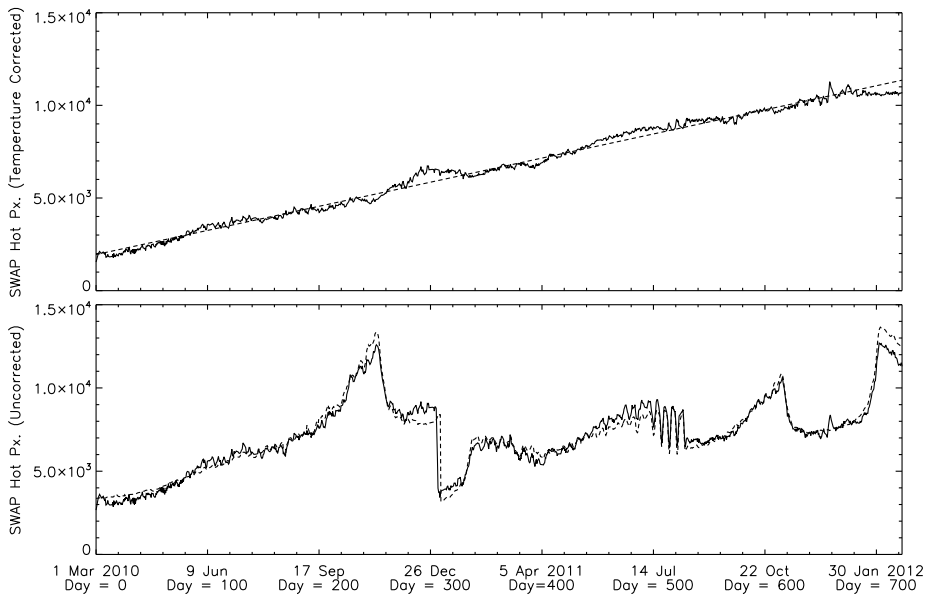
Figure 18 Spikes detected in SWAP images *versus* time. The top panel shows the rate of increase in detections with the effects of temperature variation removed. The lower panel shows the variation including temperature effects. The dotted curve in both panels shows the effect of a linear increase in spikes with a rate of 13 spikes per day. In the lower panel this has been adjusted to reflect temperature variation as well, showing that the linear increase is indeed a good match for actual detector behavior. Adapted from Halain *et al.* (2012).

day^{-1} or about 4800 spikes per year^{-1}. This corresponds to a loss of only about 0.45 % of all detector pixels per year. We note that this linear increase in pixel damage is consistent with the results of ground-based radiation exposure tests described in the detector datasheet produced by Cypress (formerly FillFactory), the detector producer. The large jump around day 300 (Figure 18 lower panel) is due to a refinement in SWAP calibration procedures. The two dips in the number of spikes near December and January 2010 and December 2011 are the result of PROBA2's reduced operating temperature during the spacecraft's eclipse season.

6.1.3. Image Quality Degradation

The final type of degradation that can affect SWAP is the degradation of intrinsic image quality due to losses of efficiency in the optical components as a result of EUV "burn-in" or deposition of contaminants on optical surfaces. This type of degradation is the most difficult to measure, since, as is the case for all space-based EUV telescopes, there is no standard EUV source available with which to measure SWAP's flat-field while in flight. However, this type of degradation was the principal cause of quality loss in images from EIT on SOHO (Clette *et al.*, 2002), which makes it worthwhile to study its role in SWAP degradation to the extent that we can do so. Although producing a true gain calibration for SWAP is very difficult, SWAP carries two visible LEDs that can help to reveal strong variations in image quality. For this analysis we compared the ratios of LED brightness at the beginning of PROBA2's mission with more recent observations of the LEDs. Since the LEDs are located close to SWAP's focal plane assembly (FPA), we cannot characterize any

changes in filter or mirror performance with this measurement. However, any significant changes in the performance of the optical path would probably be detected in our analysis of SWAP's spectral response. Nonetheless, it is worth pointing out that this analysis applies only to the FPA components and LEDs themselves. We compared LED images obtained as part of a bi-weekly calibration campaign performed throughout the mission to study changes in image quality over time. By computing the pixel-by-pixel ratio of LED images from the beginning of the mission to LED images from the end of the mission, we can determine whether any spatially coherent degradation has occurred. Comparing images from April 2012 with LED images from the early-mission commissioning phase revealed a small, ring-shaped decrease in detector response in nominal SWAP images that is roughly coincident with the location of the solar limb where the brightest coronal emission occurs. This suggests that there has been some degree of burn-in over the course of the mission. However, the decrease was only a few DN per pixel, which corresponds to a net decrease in instrumental response of less than 0.1 % of the total signal in well-exposed images. Since this level is far below instrumental noise levels and, as a result of image compression, is in fact undetectable in nominal science images, we conclude that this type of degradation is not a significant concern for SWAP. Additional discussion of the use of LED images to diagnose SWAP degradation, including a figure that shows this effect, is given by Halain *et al.* (2012).

6.1.4. Conclusion

SWAP has a dual role; it is both a scientific instrument and a test platform for new technology. While many such space-based EUV instruments have experienced significant degradation during the initial years in orbit, SWAP has shown itself to be remarkably robust against degradation of any kind. This analysis suggests SWAP has only experienced one significant type of degradation: failures in the detector electronics, which have occurred at a rate of less than 5000 out of approximately 10^6 pixels (less than 0.5 %) every year. The lessons learned from SWAP's simple, efficient, and robust design are especially applicable to instruments intended primarily for space-weather monitoring such as the proposed *EUV Solar Imager for Operations* (ESIO) instrument. Such instruments, which often are expected to operate with limited resources, must be long-lived and dependable and accordingly must be highly robust against adverse conditions in the space environment to which they will be exposed.

6.2. LYRA Degradation after Two Years in Orbit

The *Large-Yield RAdiometer* (LYRA) observes the Sun in four spectral bands that range from UV to soft X-ray. It consists of three units that are redundant but not technically identical. While each unit consists of the same four spectral channels that cover a wide emission temperature range, these channels are realized by different filter–detector combinations. Three types of detectors were used: conventional Si photodiode detectors (AXUV type from IRD) and two types of diamond detectors, which have the advantage of being radiation resistant and insensitive to visible light (BenMoussa *et al.*, 2006). Another advantage of LYRA is its high observation cadence, up to 100 Hz. LYRA uses two calibration LEDs per detector to individually monitor the possible detector degradation over the mission lifetime.

   LYRA channel 1 (Lyman α) covers a narrow band around $120 - 123$ nm, plus, unfortunately, a major contamination caused by longer wavelengths. LYRA channel 2 (Herzberg) covers the interval $190 - 222$ nm in the Herzberg continuum. LYRA channel 3 (aluminum) covers the $17 - 70$ nm Al-filter range including the strong He II 30.4 nm line and soft X-ray contribution below 5 nm. LYRA channel 4 (zirconium) covers the $6 - 20$ nm Zr-filter range

with the highest solar variability and soft X-ray contribution below 2 nm. For a detailed description of the mission, see Hochedez *et al.* (2006).

Since PROBA2 is a combined science and technology mission, the goal was not only to provide scientific data for studying solar flares, space weather, and aeronomy, but also to observe the performance of new technologies in space. Thus, the observation of the instrument's degradation and its causes is an important part of the mission goal.

6.2.1. Calibration

The spectral response of the twelve possible filter–detector combinations was tested before launch with a standard source (PTB/BESSY II); for details see BenMoussa *et al.* (2009a). The various nominal spectral intervals were defined accordingly, such that they cover at least 95 % of the response. This does not apply for the Lyman α channel, since the unwanted longer-wavelength contributions to this channel depend on the detector technology.

LYRA has been continuously observing the Sun, basically with its unit 2, for more than two years. The data presented on the PROBA2 website (proba2.sidc.be) include daily plots, three-day plots, monthly overviews, flare lists, and a comparison with the soft X-ray of NOAA's *Geostationary Operational Environmental Satellites* (GOES) satellites. LYRA data are available in daily FITS files; users can chose between uncalibrated and calibrated time series in full temporal resolution and calibrated data averaged in one-minute intervals.

6.2.2. Degradation

LYRA unit 2 consists entirely of new diamond detectors to be tested in space. It is therefore selected to be the "nominal" unit and has been used, almost without interruption, since 6 January 2010, the day that LYRA first opened its covers. Unit 1 and unit 3 are only opened and used sporadically for limited campaigns and for calibration purposes. Consequently, unit 2 degraded quite fast, especially in its longer-wavelength channels; see Figure 19.

LYRA's original spectral response, as measured in the laboratory, can only be compared in a reasonable way with other space instruments when data of the first-light day are used, *i.e.* before heavy degradation set in. It was therefore decided to calibrate LYRA with the help of a combined solar spectrum observed on 6 January 2010 by SOLSTICE onboard the *Solar Radiation and Climate* (SORCE) and the *Solar EUV Experiment* (SEE) on the TIMED mission. The calibration was then extended by adding the estimated loss by temporal degradation. This method has the advantage of leaving the flare components within the shorter-wavelength channels untouched, since it is observed that these signals do not degrade. In addition, the shorter-wavelength channels react more to long-term solar variability; therefore this variability has been adjusted with the help of ch3-4 (*i.e.* unit 3, channel 4), the zirconium channel of unit 3, which is assumed to be non-degrading.

By mid-March 2012, unit 3 had been open to the Sun for approximately 375 hours. It could thus be compared with the first 375 hours of open unit 2, which was reached around 5 February 2010, within the commissioning phase. The result is shown in Figure 20 and Table 3.

The loss percentage for the short-wavelength channels is calculated assuming that the solar irradiance had dropped by 2 % within the period covered by unit 2, and that it had increased by 55 % in the period covered by unit 3; this is observed by LYRA ch3-4 [*i.e.* unit 3–channel 4]. It is furthermore assumed that the solar variation as reflected in ch2-3, ch2-4, ch3-3, and ch3-4 is linearly dependent, and that ch3-4 is not degraded.

Figure 19 Temporal degradation and estimation of future trends for LYRA unit 2.
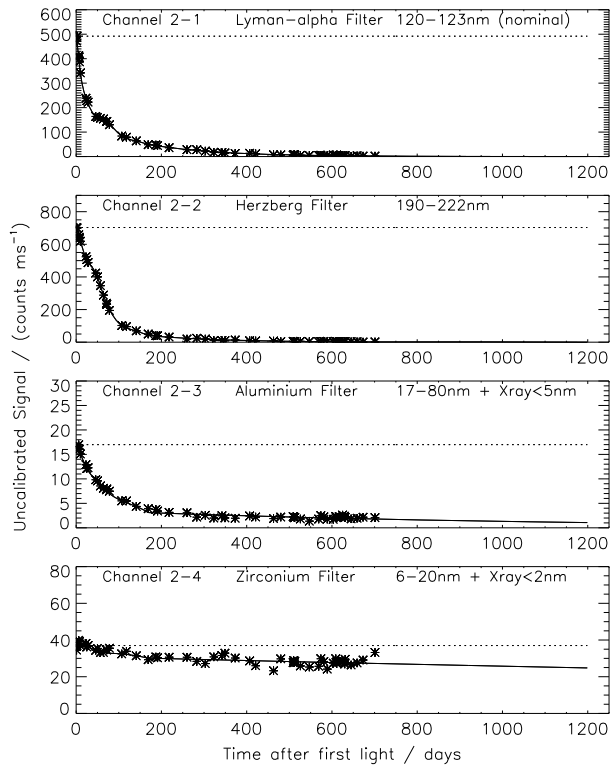

Table 3 Relative signal losses (to the output signal on 6 January 2010: first light) in the four LYRA channels of unit 2 and unit 3, each after 375 hours of open covers (dark currents subtracted). To remove the solar variation contribution in the shorter wavelengths (*), ch2-3, ch2-4, and ch3-3 were adjusted relative to ch3-4, which is assumed to be non-degrading.

LYRA-unit2	Degradation [%]	LYRA-unit3	Degradation [%]
ch2-1	58.3	ch3-1	28.3
ch2-2	32.5	ch3-2	30.9
ch2-3	28.7*	ch3-3	45.2*
ch2-4	10*	ch3-4	0*

The loss in ch3-1, a channel that has significant contributions from visible and IR radiations (Si detector), appears to be lower than in ch2-1, which only has a significant contribution from UV, apart from the Lyman α line. Ch3-3, after removal of the solar variation, initially appears to degrade as fast as the longer-wavelength channels, while channel 4 appears to degrade more slowly than the others. Meanwhile, it is observed by regular calibration campaigns – using the LEDs with covers closed – that the photodetectors made of diamond do not show any degradation, while the Si AXUV detectors show a slight increase of their dark current.

As can be seen in the unit-3 part of Figure 20, the degradation slows down after sixty hours, which corresponds to campaigns around the end of 2010, *i.e.* after approximately one year of operations.
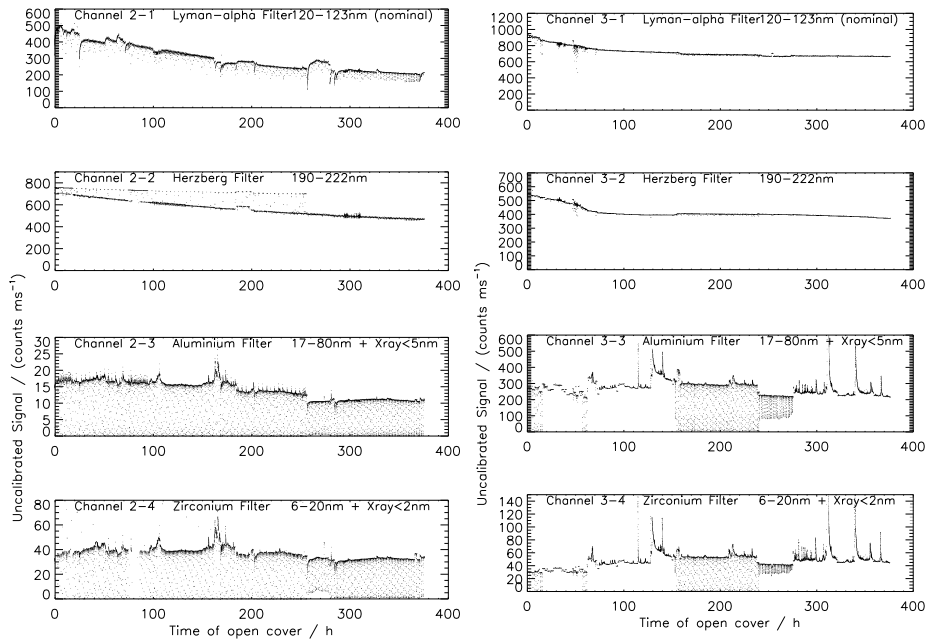
Figure 20 Comparison of the first 375 hours of unit 2 (quasi-continuous 6 January 2010 – 5 February 2010) and unit 3 (campaigns 6 January 2010 – 15 March 2012).

6.2.3. Comparison with EURECA/SOVA

Taking these results into account, the degradation of LYRA basically appears not to be caused by detector loss, but by molecular contamination on the front optical-filter surface. It is interesting to compare this with another space instrument, *Solar Oscillation and Variability* (SOVA) onboard EURECA, which experienced both kinds of losses.

The SOVA experiment has three channels at around 335 nm (UV), 500 nm (visible), and 862 nm (NIR). Its *sunphotometers* (SPM) were operated in space for eleven months on-board EURECA. SOVA was launched and retrieved with shuttles in 1992 – 1993 and was inspected at the Physikalisch-Meteorologisches Observatorium Davos/World Radiation Center after retrieval in 1994. A yellow–brownish stain of unknown composition was found on the quartz windows and the apertures. For a more detailed description, see Wehrli, Fröhlich, and Romero (1996).

The UV detectors of SOVA faced a degradation – an immediate loss of ≈ 70 % – that appeared to be caused by radiation in space, independent of open-cover duration. Indeed, high-proton energies (from the SAA) induced secondary-particle generation when passing through the cover. In this case, the cover shielding is no longer effective. This can be distinguished from the LYRA degradation and compared with the complementing LYRA channels in the UV range. Figure 21 shows the degradation of the four LYRA unit-2 channels together with the three SOVA SPM-A channels after 200 days of sunlight exposure. The solar spectra are plotted to demonstrate the places of strongest variability and the points or intervals that the LYRA and SOVA channels correspond to. The heaviest loss occurs in the UV around 200 nm; compared to this, the losses in the IR and SXR appear negligible.

By connecting LYRA and SOVA data points, we suggest that there is probably a common mechanism responsible for the degradation of LYRA and SOVA, most likely the contami-
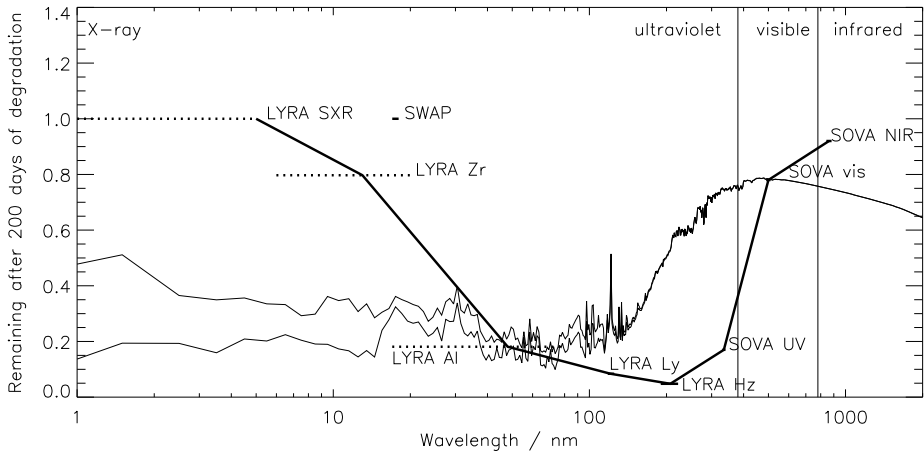
Figure 21 Normalized instrument-response degradation as experienced by LYRA and SOVA after 200 days of open covers *vs.* spectral ranges of their individual channels. The two curves show two typical solar spectra on a log–log scale in arbitrary units, one from a quiet Sun, and one from maximum sunspot activity with the Sun actively flaring.

nant deposited on the filters. The extreme degradation observed in the 20–500 nm range, mainly caused by some molecular contaminants, implies that more studies are necessary and strong requirements need to be placed on mission preparation to avoid this in future long-term UV solar observations.

LYRA appears to have avoided detector degradation by exploiting a different technology. Apart from this, the *window* degradation – obviously caused by UV-induced polymerization of contaminants on the filter surface – has remained a problem since the times of SOVA. The experience with SOHO, launched in 1995, shows that it could have been avoided with an extensive cleanliness program.

7. SDO/EVE Instrument Degradation

The *Solar Dynamics Observatory / Extreme Ultraviolet Variability Experiment* (SDO/EVE: Woods *et al.*, 2012; Didkovsky *et al.*, 2012) are solar EUV spectrometers that show degradation of the EUV signal due to various mechanisms.

The SDO/EVE instrument comprises several channels using different technologies. The *EUV spectrophotometer* (ESP) is very similar to the SEM (*cf.* Section 2.4); it uses a transmission grating and photodiodes to provide zeroth-order and first-order measurements in the bands 0–7 nm (zeroth-order), 17–22 nm, 24–28 nm, 26–34 nm, and 34–38 nm in first-order. Again an Al filter is used to restrict the bandpass incident on the grating. A separate Ti filter is used to additionally limit the bandpass seen by the zero-order detector. A Mg filter in front of the detector blocks second-order grating diffraction.

All channels of the ESP have shown degradation, as shown in Figure 22. This degradation has been shown to be due to front-filter contamination, because there are three Al filters on a filter wheel. The primary filter is used for most observations. The secondary filter is exposed for about five minutes per day to track the degradation of the primary filter, and a tertiary filter (only exposed for five minutes a week) tracks the degradation of the secondary filter. There is also a sounding-rocket campaign that provides an independent determination of

Figure 22 Degradation of the SDO-ESP channels. The ESP has three science filters in a filter wheel. By exposing the backup filters for only a very short time, the degradation of the primary filter can be measured on-orbit. The calculated degradation is checked with rocket underflights.
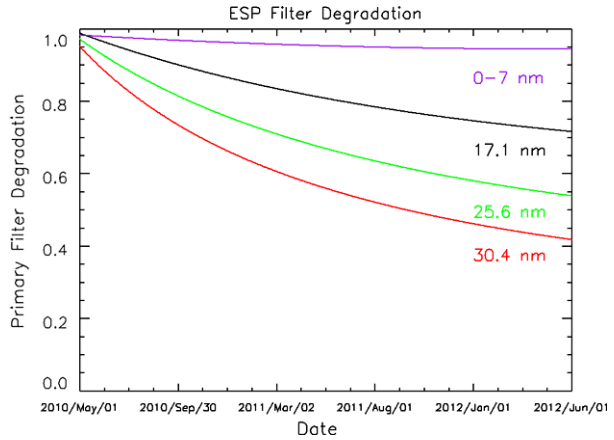

the degradation about once per year. Again, the degradation is consistent with a C layer forming on the front filter, and the thickness of C is appropriate for the degradation seen in all wavelength channels. The 36-nm channel shows a different form of degradation due to a drastic reduction in the shunt resistance of the photodiode detector. It is not known what caused this failure, but the 36-nm channel has not returned useful data since launch.

The *multiple EUV grating spectrograph* (MEGS) channels on EVE cover the $6 – 105$ nm range with 0.1 nm resolution in three bands: MEGS A1, A2, and B. MEGS A1 and A2 share a single grazing-incidence and mirror grating. Two separate slits illuminate the grating, each with separate thin-foil filter (also of each type in a filter wheel). The A1 channel is optimized for the $5 – 18$ nm range with a C–Zr–C filter. The A2 is optimized for $17 – 36$ nm with a Al–Ge–C filter. The A2 channel shows degradation very similar to that experienced by ESP (Figure 23, bottom), and a similar layer of C also explains the wavelength-dependent degradation. It is very interesting that the A1 channel (only a few mm from A2) shows insignificant degradation (Figure 23, top) even at 17 nm where the wavelength range between A1 and A2 overlaps. There must therefore be something about the filter that causes accumulated contamination on the Al filter and not on the Zr.

The MEGS-B channel is designed to operate in the $36 – 106$ nm range. It is a cross-dispersed normal-incidence spectrometer, again with a CCD detector, nominally identical to the MEGS-A detector. MEGS-B does not use a filter-wheel filter for normal operation. MEGS-B showed dramatic degradation from the NIST-calibrated response at first light. The responsivity above 60 nm showed a steady drop and is about 90 % degraded at 105 nm (Figure 24). This "first-light" degradation could not be recovered by heating the detector to $+17$ °C (as hot as possible) for several days. The degradation continues to worsen with solar exposure, and flat-field images show burn-in of the brighter lines. It is thought that this degradation is due to back-side charging of the CCD. The initial charging was caused by proton damage because SDO spent significantly longer in the geo-transfer orbit than planned, and this orbit dips into the inner proton belt twice a day, delivering a significant proton dose. The CCDs have a p-type implant to provide about a 7 nm dead layer of Si between the SiO_2/Si interface and the charge-collection region of the CCD. This was expected to provide enough isolation from back-side charging for the SDO mission life. However, once the potential due to surface charging exceeds that of the doping layer, degradation will be evident and will follow the penetration depth of Si (as seen in MEGS-B), and because the charging caused by incident photons is dependent on the exposure time, this mechanism also explains the burn-in. To maintain the sensitivity of the MEGS-B channel, it is only exposed

Figure 23 SDO/MEGS-A degradation. Top: MEGS-A1 C–Zr–C filter shows insignificant degradation. Bottom: MEGS-A2 shows degradation very similar to that of ESP. Updated from Hock (2012).
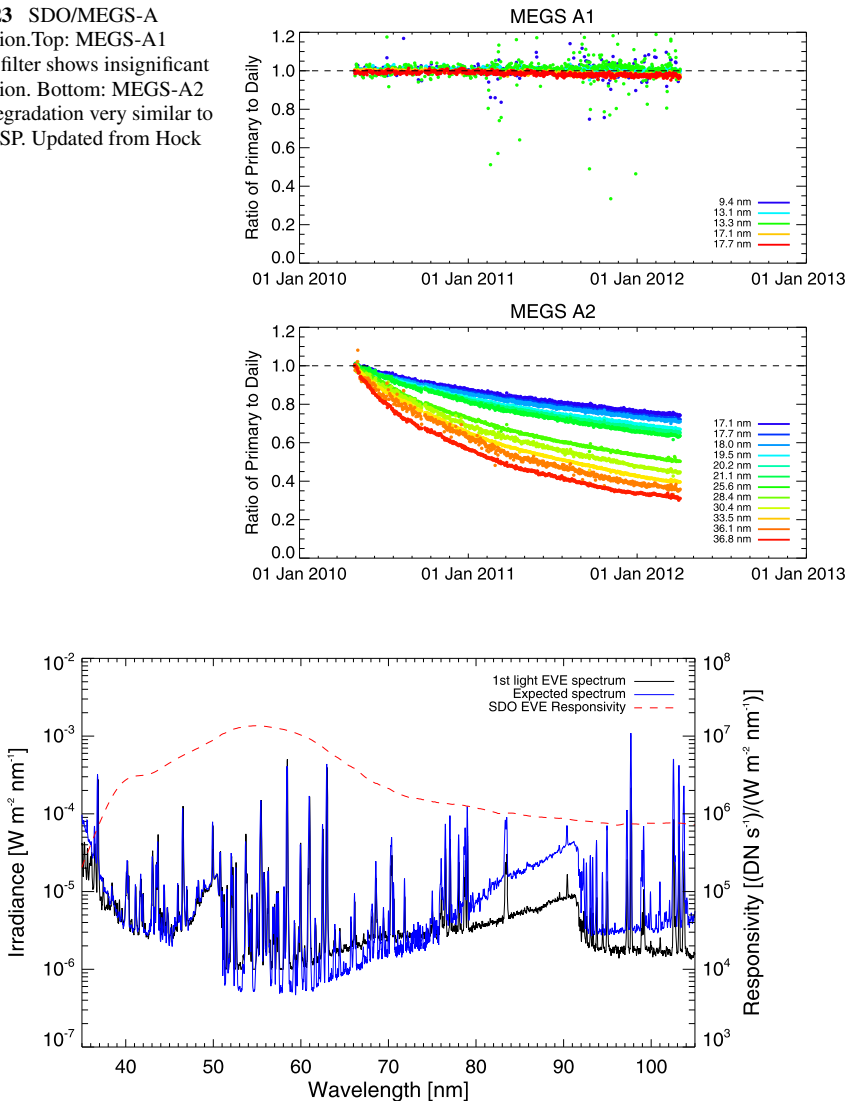
Figure 24 Degradation of the SDO/MEGS-B channel at first light. Updated from Hock (2012).

for a short time each day, although campaign modes can be organized if continuous data are required. A similar effect is just beginning to be seen in the MEGS-A CCD, especially for the 30.4-nm line. However, because the penetration depth of photons is deeper for the shorter wavelengths, the effect is much less significant.

Finally, MEGS-P is a Lyman α monitor. The zero-order from the first grating of MEGS-B is incident on an Acton 122XN interference filter to isolate the 121.6 nm Lyman α line. This is then measured by a photodiode. There is no noticeable degradation of this channel at all, which suggests that the MEGS-B first grating (exposed to the full solar spectrum) is not degrading either.

8. Solar Instruments Onboard Picard

Picard is a scientific microsatellite (140 kilograms) that was launched on 15 June 2010. *Picard* is devoted to solar-variability observation through imagery and radiometric measurements, with the aim of providing data for solar-physics investigations, and for the assessment of the influence of solar variability on the Earth's climate variability. The *PREcision MOnitoring Sensor* (PREMOS: Schmutz *et al.*, 2009) and *SOlar Diameter Imager and Surface Mapper* (SODISM: Meftah *et al.*, 2010), whose evolution is described in this article, are radiometers used to measure the solar irradiance and an imaging telescope to determine the solar diameter and asphericity, respectively.

### 8.1. Operational Modes and Degradation of PREMOS

PREMOS onboard the French satellite *Picard* comprises two experiments: one experiment is measuring the Total Solar Irradiance (TSI) with absolute radiometers, the other observes solar spectral irradiance at six different wavelengths with filter radiometers (given in Table 4). We report below on the second experiment. The optical and near-IR filters are identical to those in the *Picard*/SODISM instrument and the 215-nm filter, while the 210-nm filter was chosen to match the Herzberg channel implemented on the PROBA2/LYRA instrument. The PREMOS filter radiometer therefore covers an important part of the spectral range that influences the chemical composition of the terrestrial atmosphere. The operational routines began on 6 September 2010, and PREMOS filter radiometers have provided continuous data since, even during the eclipse season. Using a total of twelve channels divided into three instruments of four channels, a redundancy strategy has been established to estimate sensitivity loss due to exposure time to sunlight.

One channel (Head A) is operated continuously (six measurements per minute with an integration time of 9.9 seconds for the normal mode), while its back-up channel (Head C) is exposed only once per day for three minutes. Finally, the Head B channel is a self-consistent system with duplicate channels; the first pair is exposed every fourth orbit for one minute, while the second pair is exposed once per week for about two minutes.

As displayed in Figure 25, Head A has experienced a pronounced degradation since it has lost more than 99 % of the signal for the UV channels and about 35 % for the visible channel, while more than 86 % of the signal remains for the near-IR channel. We assume that this degradation is induced by the polymerization of contaminants on top of filters under the solar UV exposure. We are currently investigating why the degradation is not a decreasing function for the visible and near-IR channels. Head C has been exposed for only 40 hours since the beginning of the mission. For the UV channels (Head C), we estimate the loss of sensitivity to be about 10 % and 5 %, respectively. It is much more difficult, however, to estimate the degradation of the visible and near IR channels. The operational channels of Head B have been exposed to the Sun for approximately sixty hours, while the back-up channels have been exposed for less than four hours. We are currently using the channels of Head B to model the degradation for all UV channels.

8.2. Aging of the Picard Payload Thermal Control: Impact on SODISM

SODISM is an 11-centimeter Ritchey–Chretien imaging telescope developed by the French Centre National de la Recherche Scientifique (CNRS). SODISM measures the solar diameter and limb shape and performs helioseismic observations to probe the solar interior. The solar diameter is measured at three wavelengths in the photospheric continuum, *i.e.* 535,
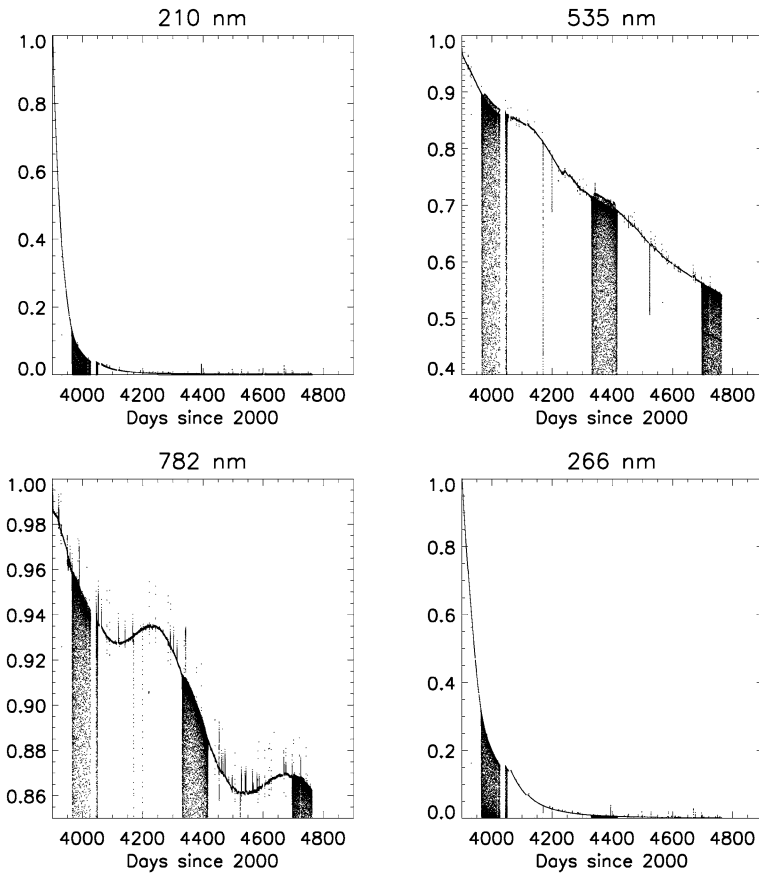
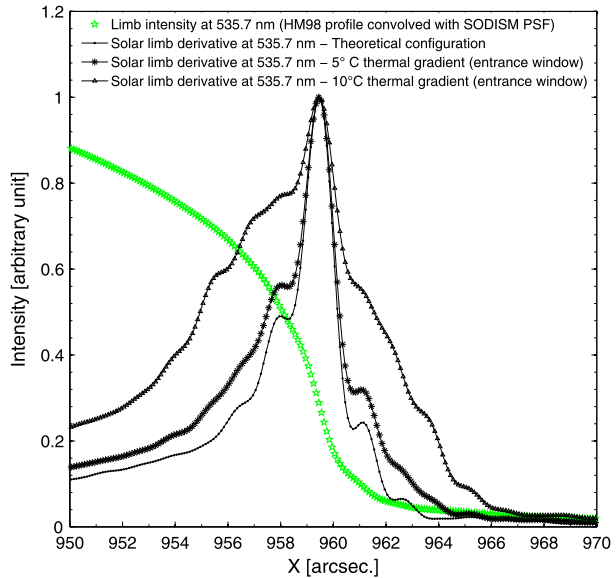**Figure 25** Normalized time series for all channels of Head A since the beginning of the *Picard* mission.

Table 4 Wavelength characteristics of the PREMOS filter radiometers.

	Channel 1	Channel 2	Channel 3	Channel 4
HEAD A	210 nm	535 nm	782 nm	266 nm
HEAD B	215 nm	607 nm	215 nm	607 nm
HEAD C	210 nm	535 nm	782 nm	266 nm

607, and 782 nm. Images in the Ca II line (393 nm) are used to detect active regions near the solar limb that could alter the diameter measurements. These images are also used to measure the solar differential rotation and to monitor space weather, together with images at 215 nm.

Throughout the mission, thermal control ensures that each instrument or equipment unit is maintained at temperatures consistent with nominal operation. Most of the instruments only operate correctly if maintained at the right temperature and if temperature changes are within acceptable limits. Thermal-control surfaces and optics of the payload are exposed to space environmental effects including contamination, atomic oxygen, UV radiation, and vacuum temperature cycling. The elements of SODISM that are regulated and not exposed to

Figure 26 Thermal effect on the solar limb measurement at 535.7 nm.

Legend:
- ★ Limb intensity at 535.7 nm (HM98 profile convolved with SODISM PSF)
- Solar limb derivative at 535.7 nm – Theoretical configuration
- Solar limb derivative at 535.7 nm – 5° C thermal gradient (entrance window)
- Solar limb derivative at 535.7 nm – 10°C thermal gradient (entrance window)

the Sun (*e.g.* CCD, interference filters, mechanism, structure) remain stable with changes in temperature. In flight, the temperature of the SODISM's CCD (2028×2048) is very stable, within 0.1 °C.

Materials with low solar absorptance are often used for reflective surfaces designed to minimize heat absorption, but UV radiation degrades these materials by exponentially increasing the solar absorptivity of exposed surfaces. The contamination on thermal control surfaces alters absorptance/emittance ratios and changes the thermal balance, which leads to an increase of the payload temperature. Contamination in optical instruments, on the other hand, reduces the signal throughput, which in turn reduces the performance even more. The *Picard* payload thermal-control system includes several temperature-control techniques, such as reflective covers, coatings, insulation, and heat sinks. Aging of the covers, coatings, and insulation was observed and expected to be cumulative with time. The SODISM entrance window and the front of the instrument facing the Sun have a significant temperature increase. A general aging of the thermal-control system is observed as well.

The temperature of the SODISM front face varies greatly during an orbit and its temperature variation strongly depends on latitude and on the day of the year (variation and effect of incident fluxes). This temperature evolution of the instrument front face principally impacts the main entrance window and considerably degrades the measurement of the intensity profile's first derivative at the solar limb, and consequently the measurement of the solar limb as illustrated in Figure 26.

Despite the establishment of an active thermal control, there are also environmental effects on the SODISM instrument. We observed that the CCD is strongly affected by the SAA. The SODISM image intensity (normalized to 1 AU) is shown in Figure 27 and evolves over time with

- intensity oscillation at 535.7 nm, 607.1 nm, and 782.2 nm,
- intensity oscillation and significant degradation at 215 nm and 393.37 nm.

These effects might be caused by a combination of contamination and degradation at the detector surface. To outgas the accumulated contaminant on the CCD surface, a bake-out
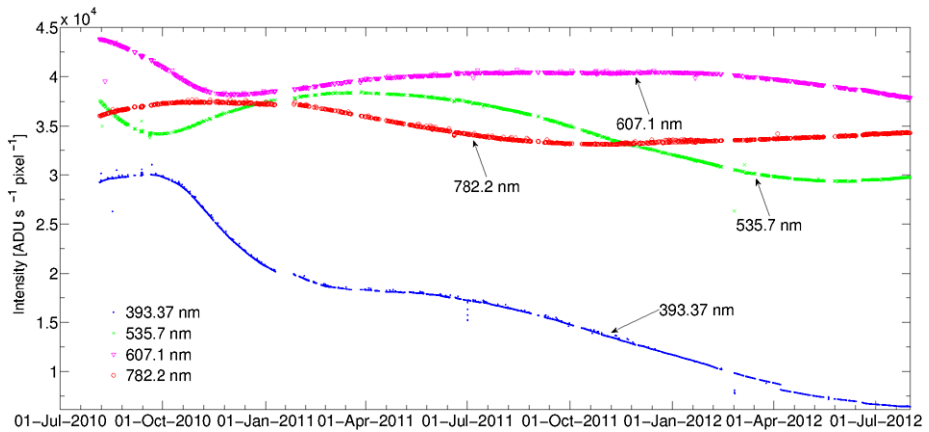
Figure 27 Temporal evolution of the SODISM CCD image intensity.

heater is installed on SODISM; this allowed periodic heating to $+20$ °C during three days, but it was not effective. Another approach should be developed.

Thermal control, especially for a payload suite, is crucial to mission success. For SODISM, a deterioration of the thermal-control system was observed in the long term (in particular in the front face of the telescope). The measurements show a complex behavior with thermal and contamination effects as well. For the long-term evolution on SODISM measurements, we suspect a degradation of its CCD response, caused by contamination and energetic-particle issues, and transmission filters at the entrance window of SODISM. Up to now, there is a good repeatability in measurements but most of the calibration requires thermal and/or optical corrections. Thermal coatings chosen for the *Picard* payload are adequate for maintaining temperatures in the acceptable range, but the use of radiators (white paints) facing the Sun is not a proper solution, a Sun shield with back-surface mirror should be used. Moreover, metrology missions, such as *Picard*, require more dimensionally stable spacecraft structures. Because there is a strong effect between the latitude and the measurement of the solar radius, low-mass spacecraft in low orbits should be avoided.

9. Lessons Learned and Recommendations

The degradation of space instruments can be complex; their causes and mechanisms are, in many instances, difficult to understand, since they are often the result of a combination of several independent degradation processes. This fact is an especially important issue in establishing recommendations for best practices in developing and operating spaced-based solar instruments. However, as demonstrated by the contributions of this article, the presence of contaminant species (organics and water) and exposure to radiation (both ionization and displacement-damage effects) are often the main reason for instrument degradation, and their impact is frequently underestimated. Contaminants can originate not only from spacecraft propellant, but also from outgassing or evaporation by all organic material used in the construction of these instruments. Furthermore, once instruments are in space, the means to recover from degradation are very limited. For example, items that have collected contaminants while operating under cryogenic temperatures can be heated – to an extent limited by electrical power available – to desorb weakly bound molecules. However, once molecules

have settled by UV-polymerization, cleaning is very nearly impossible. Although methods to recover from degradation have been established and have successfully been used in the laboratory such as UV-ozone cleaning, such a method has not been implemented in a space mission. Currently, there is no alternative to mitigating contamination in space.

Our survey showed that three complementary strategies can dramatically minimize degradation and mitigate the effects of ongoing degradation:

- ensuring extreme cleanliness control during instrument development and launch, including careful material selection, minimization of organic material, and conditioning by bake-out,
- monitoring the stability of the radiometric calibration using sophisticated methods,
- identifying development needs for critical components (imagers, photodetectors, optics, coating, electronics, *etc.*).

9.1. Extreme Cleanliness Control

The cleanliness efforts for SOHO described in Section 2 were very successful; they were not excessive, but neither were they completely perfect. This became evident when the SOHO spacecraft was lost and then recovered after four months in 1998. As the inter-calibration observations were resumed after the recovery of SOHO, the degradation corrections for several instruments had to be completely remeasured because the temperature excursions during the phase of uncontrolled thermal environment released contaminants that had been residing for a long time on cold surfaces and resulted in a redistribution of contaminants and, thus, accelerated instrumental degradation that had now to be taken into account. So, while contaminants were still present onboard, the on-ground cleanliness activities reduced the potential for degradation considerably.

Our conclusion is, therefore, that stringent cleanliness efforts are an absolute prerequisite for calibration stability. The main ingredients of a successful cleanliness program are the establishment of a cleanliness review board, inter-calibration working group, and instrument and spacecraft cleanliness control plans.

The most important preventive measures for space instruments identified were

i) Determining the contamination sensitivity (also at spacecraft level) by modeling,
ii) Design of the instrument to maximize cleanliness,

- including design features such as purging concepts with large venting holes in the structural housing, the addition of vents and heaters close to the detector for bake-out ($> +35\,°C$), door mechanisms, filter wheels with redundant filters to track front-filter contamination, contamination sensors (QCM), cold cup around the detector, solar-wind deflector plates, valves for depressurization during launch, *etc.*
- selecting high-radiation-tolerance and ultra-high vacuum quality materials with the lowest outgassing values available (the total mass loss [TML] and the collected volatile condensable materials [CVCM] plus an additional parameter: the water vapor regained [WVR]).

iii) Stringent cleanliness procedures of all hardware:

- assembly in cleanroom (class ISO 5) with active charcoal filters,
- use of oil-free vacuum systems during tests,
- double bagging and continuous purging with pure and dry N_2 (grade 5.0) at instrument level up to the launch.

iv) Extensive use of vacuum bake-outs at the component, sub-assembly, and final-assembly level:

- baking at the highest temperature ($> +100$ °C) compatible with the material under clean-gas purging,
- bake-out durations determined by mass spectrometer and temperature-controlled QCM monitoring of cleanliness level,
- gas-chromatography/mass spectrometry (GC/MS) analysis for acceptance/rejection of the components.

It should be added that the ground-support equipment that will be in direct contact with the flight hardware must be submitted to the same rules. As an example, cleanliness of vacuum chambers must be monitored by QCM or residual-gas analyzers.

9.2. Stability of the Instrument Radiometric Calibration

The careful and extensive radiometric calibration of the instruments prior to launch forms the basis of the success of spaced-based solar instruments. In most cases, opportunities for instrument-level tests and calibration are strongly limited by pre-launch scheduling constraints, but this testing is important enough to warrant special consideration. Pre-flight calibration can be achieved with detectors and transfer radiation-source standards, both traceable to a primary standard source found in synchrotron-radiation facilities, while the instruments themselves can be calibrated at the synchrotron facility or locally, at the instrument test facility, by transporting a transfer source standard to that facility. The latter option additionally reduces the possibility of contamination by exposing the instrument to an environment whose cleanliness cannot be sufficiently regulated.

Once a spacecraft is in orbit, the stability of calibration can be monitored by carefully planned observations, but absolute calibration is often impossible. Consequently, a careful initial calibration and meticulous tracking of the evolution of instrumental calibration are both very important. Several different methods of calibration may be required to achieve this goal (Schühle *et al.*, 2002). Furthermore, qualified personnel and perhaps external expertise are often useful in interpreting the obtained data, both on the ground and in-flight, to accurately assess the degradation evolution of a space-based solar instrument.

9.2.1. Onboard Calibration

Onboard-calibration light sources have been essential to the success of many solar payloads, and similar devices should always be included in the design of space-based solar instruments. Multiple calibration light sources (lamps or LEDs) may be carried onboard and should be operated and exposed regularly to maintain an established calibration status. It is worth noting that the value of calibration light sources is significantly reduced without pre-flight or pre-degradation reference data obtained during the on-ground calibration and in-flight commissioning phases of the mission.

However, for EUV–VUV and X-ray instruments, for which calibration sources in the primary range of EUV instrumental sensitivity are not available, the onboard visible-light flat-field that these onboard light sources provide can be used to monitor instrumental degradation if the relationship between visible and EUV degradation is known. Although such lamps were used with great success in the in-flight calibration of EIT, these successes seem to be the exception rather than the rule. Ideally, however, it should be possible to establish the relationship between visible and EUV degradation, as well as the degradation potential

of the light sources themselves, before flight by irradiating engineering devices. Additionally, we strongly recommend the use of blue or near-UV LEDs that have photon penetration depths similar to or lower than the EUV photons observed by the instrument, and that every effort should be made to ensure complete and uniform detector illumination by these lamps on future EUV telescopes.

9.2.2. Calibration Updates and Inter-Calibration

Alternatively, it is possible to track instrumental calibration by inter-calibration using observations from occasional rocket underflights using similar instruments that can be carefully calibrated on the ground both before and after the flight. Another option for establishing absolute calibration using in-flight observations are invariant sources – assuming they are accessible by the instrument – such as observations of celestial standard sources or of the Sun-center during quiet periods, or by inter-calibrating identical variable sources using different instruments with a similar corresponding wavelength sensitivity. In the case of visible-light imaging instruments, observations of the background star field can also be used to monitor long-term degradation, as has been done very successfully in the case of STEREO/SECCHI's HI-1 imager. However, for inter-calibration measurements, off-point and roll maneuvers of the spacecraft platform may be required to correct for the effects of spatial and spectral dependent degradation patterns (*i.e.* flat field and stray light).

9.2.3. Redundancy Concept

Redundancy can be implemented at either component or instrument levels (such as LYRA and PREMOS). Past experience shows that redundancy is useful in recovery from degradation and damage from different causes. For example, the degradation of thin-film filters typically occurs during launch, but impact by debris or micrometeoroids (see, for example, EIT) can cause irreparable damage if redundant parts are not available. For radiometers, the use of several spare units – the number may depend on the projected lifetime of the mission – with separate door covers is strongly recommended. In addition to protecting against potential single-unit failures, observations by less-exposed units with a low duty-cycle – for example, a few minutes per week – can provide valuable information on the long-term evolution of the instrument.

9.3. Identification of Development Needs

Specific design and technological development is particularly important for UV instruments. For the SOHO UV instruments, the optical systems were quite stable during flight (Schühle, 2003), but the detectors remained a source of instability (Thompson, 1999). This was due partly to the temperatures of CCD detectors and partly to the effect of irradiation on the Si devices, while detectors with multichannel-plate intensifiers suffered from gain depletion during exposures.

This detector-degradation problem is frequently predicted before launch, but both its importance and severity are often underestimated. A list of all proven technologies and their degradation levels is beyond the scope of this article, but one especially important recommendation concerns the use of back-illuminated detectors, which affects both CCDs and CMOS APS detectors. The commonly used detector interface (Si/SiO_2) is very sensitive to radiation damage (both by protons and UV photons) in space, which leads to a decline in detector sensitivity over time. However, proper surface passivation of the backside of existing

detectors can reduce the impact of radiation exposure, and intensive pre-flight characterization can help to mitigate the damage that cannot be controlled. It would be worthwhile to explore the use of alternative oxides with greater radiation tolerance (*e.g.* Al_2O_3) and non-oxide passivation layers.

In most cases, CCDs should be kept at the lowest possible operating temperature to reduce dark current, the effects of radiation damage, and the appearance of *hot, warm*, and *flipping* pixels. Our analysis suggests that operating temperatures should be lower than $-60\,°C$ for non-inverting mode operation (NIMO) or $-40\,°C$ for asymmetric inverting mode operation (AIMO) CCDs.

Finally, even while research and development in space technology is widely acknowledged as essential for designing future long-lifetime space missions, we recommend intensified efforts to develop advanced photon radiation detection systems, in particular those described below.

9.3.1. Next-Generation CMOS-APS

We expect that many future instruments will make use of highly efficient CMOS-APS detectors similar to the one used by SWAP. In fact, the *Extreme Ultraviolet Imager* (EUI), the *Heliospheric Imager* (SoloHI), and the *Polarimetric and Helioseismic Imager* (PHI) onboard the *Solar Orbiter* mission are all expected to incorporate the next-generation of CMOS-APS detectors with significantly improved characteristics (see BenMoussa *et al.*, 2013 for the detector prototype development of EUI).

9.3.2. Thoroughly Tested UV Filters

There is a great need for optical elements of all kinds (filters, grazing reflectors, and mirrors) with improved radiation tolerance and spectral purity. This need is demonstrated by the rapid degradation of the UV filters on PROBA2 and *Picard*. For successful future missions, modeling and complete test campaigns for UV and visible filters (including radiation and contamination simulations tests) are basic requirements.

9.3.3. Radiation-Hardened UV-Sensitive Materials

Radiation hardness against UV photons or protons is another primary concern for upcoming long solar missions that will remain in space for several years. There are promising alternatives to the commonly used silicon-based imagers and photodetectors based on wide bandgap materials such as the diamond detectors used in LYRA. Details of these next-generation detectors are discussed by BenMoussa *et al.* (2009b). A proof-of-concept AlGaN imager (256×256 pixels), sensitive only to UV and operating at room temperature, has been recently reported by the *Blind to Optical Light Detectors* project (BOLD: Malinowski *et al.*, 2011).

9.3.4. Onboard Data Processing

Given the issues that remain in providing high data-flow for nearly all space-based instruments, and, in particular, issues with the optimization of data-flow for spacecraft in low-telemetry orbits, future systems must be capable of high-performance onboard computing, which in turn requires high-performance, radiation-hardened, field-programmable gate arrays (FPGAs) that can perform automated onboard calibration. For some missions it will be necessary to update detector-calibration maps and perform onboard image correction such as high-quality cosmic-ray removal in order to prevent unrecoverable distortion caused by low-quality image compression or a very poor lossless compression ratio.

10. Conclusion

The workshop that took place in the Solar Terrestrial Centre of Excellence (STCE) in Brussels, Belgium on 3 May 2012 provided an excellent starting point for a dialog between experts and facilitated the exchange of much experience gained during space-based solar missions. The outcomes of this meeting and discussion, together with the written contributions of the different mission teams, have sparked this article which focused on the main lessons learned about in-orbit degradation of solar instruments.

Although this article addressed scientists and, perhaps more specifically, engineers involved in spaced-based solar-instrument development, all stakeholders of any project should be deeply involved in assessing and monitoring any degradation, and because the consequences of degradation can be quite severe, this problem should be taken extremely seriously.

There are several approaches to assessing and monitoring the degradation of spaced-based solar instruments that give good results, many of which we have discussed above. A prime conclusion of this work is that there is no single best method, but rather that a combination of methods must be critically selected, taking into account the applicability of the methods given the mission targets and the instrumental design itself. It is therefore important to continue to share regular and open information about what is working and what is not, so that we can all learn from the community's shared experiences.

In particular, identifying the lessons learned from past projects is of special value to the community and instrument teams themselves. Unfortunately, project teams often move quickly from project to project, and identifying the lessons learned rarely seems to be a priority. With this article, we hope to address this problem directly. We have identified the lessons learned by a broad range of instruments and missions that comprise a vast range of solar-physics objectives and span nearly two decades of experience. We hope that these lessons can be ingested by new instrument-development teams and, in turn, can prevent current and future missions from repeating past mistakes. It is the motivation of each individual (scientist and engineers) to learn, share, and change, which is what makes the lesson learned successful. Prevention is far better and much cheaper than cure.

References

BenMoussa, A., Hochedez, J.F., Schühle, U., Schmutz, W., Haenen, K., Stockman, Y., Soltani, A., Scholze, F., Kroth, U., Mortet, V., Theissen, A., Laubis, C., Richter, M., Koller, S., Defise, J.-M., Koizumi, S.: 2006, *Diam. Relat. Mater.* **15**, 802.

BenMoussa, A., Dammasch, I.E., Hochedez, J.F., Schühle, U., Koller, S., Gillotay, D., Stockman, Y., Scholze, F., Richter, M., Kroth, U., Laubis, C., Dominique, M., Kretzschmar, M., Mekaoui, S., Gissot, S., Theissen, A., Giordanengo, B., Bolsée, D., Hermans, C., Gillotay, D., Defise, J.-M., Schmutz, W.: 2009a, *Astron. Astrophys.* **508**, 1085.

BenMoussa, A., Soltani, A., Schühle, U., Haenen, K., Chong, Y.M., Zhang, W.J., Dahal, R., Jiang, H.X., Bolsée, D., Hermans, C., Richter, M., Kroth, U., Giordanengo, B., Barkad, H.A., Mortet, V., De Jaeger, J.C., Scholze, F., Hochedez, J.F.: 2009b, *Diam. Relat. Mater.* **18**, 860.

BenMoussa, A., Giordanengo, B., Gissot, S., Meynants, G., Wang, X., Wolfs, B., Bogaerts, J., Schühle, U., Berger, G., Gottwald, A., Laubis, C., Kroth, U., Scholze, F.: 2013, *IEEE Trans. Electron Devices*, in press.

Bewsher, D., Brown, D.S., Eyles, C.J., Kellett, B.J., White, G.J., Swinyard, B.: 2010, *Solar Phys.* **264**, 433. ADS:2010SoPh..264..433B, doi:10.1007/s11207-010-9582-8.

Bewsher, D., Brown, D.S., Eyles, C.J.: 2012, *Solar Phys.* **276**, 491. ADS:2012SoPh..276..491B, doi:10.1007/s11207-011-9874-7.

Brekke, P., Thompson, W.T., Woods, T.N., Eparvier, F.G.: 2000, *Astrophys. J.* **536**, 959.

Clette, F., Hochedez, J.-F., Newmark, J.S., Moses, J.D., Auchère, F., Defise, J.-M., Delaboudinière, J.-P.: 2002, In: Pauluhn, A., Huber, M.C.E., von Steiger, R. (eds.) *The Radiometric Calibration of SOHO, ISSI* **SR-002**, ESA, Nordwijk, 121.

Crommelynck, D.A.: 1982, In: Hall, J.B. Jr. (ed.) *Fundamentals of Absolute Pyroheliometry and Objective Characterization, Earth Radiation Science Seminars* **CP-2239**, NASA, Lougley 53.

Crommelynck, D.A., Dewitte, S.: 1999, *Adv. Space Res.* **24**, 195.

Culhane, J.L., Harra, L.K., James, A.M., Al-Janabi, K., Bradley, L.J., Chaudry, R.A., Rees, K., Tandy, J.A., Thomas, P., Whillock, M.C.R., Winter, B., Doschek, G.A., Korendyke, C.M., Brown, C.M., Myers, S., Mariska, J., Seely, J., Lang, J., Kent, B.J., Shaughnessy, B.M., Young, P.R., Simnett, G.M., Castelli, C.M., Mahmoud, S., Mapson-Menard, H., Probyn, B.J., Thomas, R.J., Davila, J., Dere, K., Windt, D., Shea, J., Hagood, R., Moye, R., Hara, H., Watanabe, T., Matsuzaki, K., Kosugi, T., Hansteen, V., Wikstol, O.: 2007, *Solar Phys.* **243**, 19. ADS:2007SoPh..243...19C, doi:10.1007/s01007-007-0293-1.

Defise, J.-M.: 1999, PhD thesis, Univ. de Liège.

Defise, J.-M., Clette, F., Moses, J.D., Hochedez, J.-F.E.: 1997, *Proc. SPIE* **3114**, 598.

De Groof, A., Berghmans, D., Nicula, B., Halain, J.-P., Defise, J.-M., Thibert, T., Schühle, U.: 2008, *Solar Phys.* **249**, 147. ADS:2008SoPh..249..147G, doi:10.1007/s11207-008-9175-y.

Delaboudinière, J.P., Artzner, G.E., Brunaud, J., Gabriel, A.H., Hochedez, J.F., Millier, F., *et al.*: 1995, *Solar Phys.* **162**, 291. ADS:1995SoPh..162..291D, doi:10.1007/BF00733432.

Del Zanna, G., Andretta, V.: 2011, *Astron. Astrophys.* **528**, A139.

Del Zanna, G., Bromage, B.J.I., Landi, E., Landini, M.: 2001, *Astron. Astrophys.* **379**, 708.

Del Zanna, G., Andretta, V., Chamberlin, P.C., Woods, T.N., Thompson, W.T.: 2010, *Astron. Astrophys.* **518**, A49.

Dewitte, S., Crommelynck, D., Joukoff, A.: 2004, *J. Geophys. Res.* **109**, 2102.

Didkovsky, L., Judge, D., Wieman, S., Woods, T., Jones, A.: 2012, *Solar Phys.* **275**, 145.

Eyles, C.J., Harrison, R.A., Davis, C.J., Waltham, N.R., Shaughnessy, B.M., Mapson-Menard, H.C.A., Bewsher, D., Crothers, S.R., Davies, J.A., Simnett, G.M., Howard, R.A., Moses, J.D., Newmark, J.S., Socker, D.G., Halain, J.-P., Defise, J.-M., Mazy, E., Rochus, P.: 2009, *Solar Phys.* **254**, 387. ADS:2009SoPh..254..387E, doi:10.1007/s11207-008-9299-0.

Fehlmann, A., Kopp, G., Schmutz, W., Winkler, R., Finsterle, W., Fox, N.: 2012, *Metrologia* **49**, 34.

Fleck, B., Domingo, V., Poland, A.: 1995, *Solar Phys.* **162**.

Fröhlich, C.: 2003, *Metrologia* **40**, 60.

Fröhlich, C.: 2012, *Surv. Geophys.* **33**, 453.

Fröhlich, C., Romero, J., Roth, H., Wehrli, C., Andersen, B.N., Appourchaux, T., Domingo, V., Telljohann, U., Berthomieu, G., Delache, P., Provost, J., Toutain, T., Crommelynck, D.A., Chevalier, A., Fichot, A., Dappen, W., Gough, D., Hoeksema, T., Jimenez, A., Gomez, M.F., Herreros, J.M., Cortés, T.R., Jones, A.R., Pap, J.M., Willson, R.C.: 1995, *Solar Phys.* **162**, 101. ADS:1995SoPh..162..101F, doi:10.1007/BF00733428.

Golub, L., Deluca, E., Austin, G., Bookbinder, J., Caldwell, D., Cheimets, P., *et al.*: 2007, *Solar Phys.* **243**, 63. ADS:2007SoPh..243...63G, doi:10.1007/s11207-007-0182-1.

Gottwald, A., Kroth, U., Richter, M., Schöppe, H., Ulm, G.: 2010, *Meas. Sci. Technol.* **21**, 125101.

Halain, J.-P., Berghmans, D., Seaton, D.B., Nicula, B., De Groof, A., Mierla, M., Mazzoli, A., Defise, J.-M., Rochus, P.L.: 2012, *Solar Phys.* doi:10.1007/s11207-012-0183-6.

Harrison, R.A., Sawyer, E.C., Carter, M.K., Cruise, A.M., Cutler, R.M., Fludra, A., Hayes, R.W., Kent, B.J., Lang, J., Parker, D.J., *et al.*: 1995, *Solar Phys.* **162**, 233. ADS:1995SoPh..162..233H, doi:10.1007/BF00733431.

Hochedez, J.-F., Schmutz, W., Stockman, Y., Schühle, U., BenMoussa, A., Koller, S., Haenen, K., Berghmans, D., Defise, J.-M., Halain, J.-P., Theissen, A., Delouille, V., Slemzin, V., Gillotay, D., Fussen, D., Dominique, M., Vanhellemont, F., McMullin, D., Kretzschmar, M., Mitrofanov, A., Nicula, B., Wauters, L., Roth, H., Rozanov, E., Ruedi, I., Wehrli, C., Soltani, A., Amano, H., Van der Linden, R., Zhukov, A., Clette, F., Koizumi, S., Mortet, V., Remes, Z., Petersen, R., Nesladek, M., D'Olieslaeger, M., Roggen, J., Rochus, P.: 2006, *Adv. Space Res.* **37**, 303.

Hock, R.A.: 2012, Ph.D., University of Colorado, Boulder.

Hock, R.A., Eparvier, F.G.: 2008, *Solar Phys.* **250**, 207. ADS:2008SoPh..250..207H, doi:10.1007/s11207-008-9203-y.

Hollandt, J., Schühle, U., Paustian, W., Curdt, W., Kühne, M., Wende, B., Wilhelm, K.: 1996, *Appl. Opt.* **35**, 5125.

Howard, R.A., Moses, J.D., Vourlidas, A., Newmark, J.S., Socker, D.G., Plunkett, S.P., Korendyke, C.M., Cook, J.W., Hurley, A., Davila, J.M., Thompson, W.T., St Cyr, O.C., Mentzell, E., Mehalick, K., Lemen,

J.R., Wuelser, J.P., Duncan, D.W., Tarbell, T.D., Wolfson, C.J., Moore, A., Harrison, R.A., Waltham, N.R., Lang, J., Davis, C.J., Eyles, C.J., Mapson-Menard, H., Simnett, G.M., Halain, J.P., Defise, J.M., Mazy, E., Rochus, P., Mercier, R., Ravet, M.F., Delmotte, F., Auchere, F., Delaboudiniere, J.P., Bothmer, V., Deutsch, W., Wang, D., Rich, N., Cooper, S., Stephens, V., Maahs, G., Baugh, R., McMullin, D., Carter, T.: 2008, *Space Sci. Rev.* **136**, 67.

Judge, D.L., McMullin, D.R., Ogawa, H.S., Hovestadt, D., Klecker, B., Hilchenbach, M., Mobius, E., Canfield, L.R., Vest, R.E., Watts, R., Tarrio, C., Kuhne, M., Wurz, P.: 1998, *Solar Phys.* **177**, 161–173. ADS:1998SoPh..177..161J, doi:10.1023/A:1004929011427.

Klein, K., Brandt, G., Fliegauf, R., Hoehl, A., Müller, R., Thornagel, R., Ulm, G., Abo-Bakr, M., Feikes, J., v. Hartrott, M., Holldack, K., Wüstefeld, G.: 2008, *Phys. Rev. Spec. Top., Accel. Beams* **11**, 110701.

Kopp, G., Lean, J.L.: 2011, *Geophys. Res. Lett.* **38**, 1706.

Kopp, G., Harber, D., Heuerman, K.: 2011 In: *AGU Fall Meeting Abstracts*, A910.

Kuhn, J.R., Loranz, D.: 1991, *Pub. Astron. Soc. Pac.* **103**, 1097.

Kuin, N.P.M., Del Zanna, G.: 2007, *Solar Phys.* **242**, 187. ADS:2007SoPh..242..187K, doi:10.1007/s11207-007-0306-7.

Lang, J., Kent, B.J., Breeveld, A.A., Breeveld, E.R., Bromage, B.J.I., Hollandt, J., *et al.*: 2000, *J. Opt. A, Pure Appl. Opt.* **2**, 88.

Lang, J., Thompson, W.T., Pike, C.D., Kent, B.J., Foley, C.R.: 2002, In: Pauluhn, A., Huber, M.C.E., von Steiger, R. (eds.) *The Radiometric Calibration of SOHO, ISSI* **SR-002**, ESA, Nordwijk, 105.

Lemaire, P.: 2002, In: Pauluhn, A., Huber, M.C.E., von Steiger, R. (eds.) *The Radiometric Calibration of SOHO, ISSI* **SR-002**, ESA, Nordwijk, 265.

Livingston, W., Wallace, L., White, O.R., Giampapa, M.S.: 2007, *Astrophys. J.* **657**, 1137.

Livingston, W., White, O.R., Wallace, L., Harvey, J.: 2010, *Mem. Soc. Astron. Ital.* **81**, 643.

Llebaria, A., Lamy, P., Danjurd, J.-F.: 2006, *Icarus* **182**, 281.

Malinowski, P.E., Duboz, J.-Y., De Moor, P., John, J., Minoglou, K., Srivastava, P., Semond, F., Frayssinet, E., Giordanengo, B., BenMoussa, A., Kroth, U., Gottwald, A., Laubis, C., Mertens, R., Van Hoof, C.: 2011, *IEEE Electron Device Lett.* **32**, 1561.

McMullin, D.R., Judge, D.L., Hilchenbach, M., Ipavich, F., Bochsler, P., Wurz, P., Burgi, A., Thompson, W.T., Newmark, J.S.: 2002, In: Pauluhn, A., Huber, M.C.E., von Steiger, R. (eds.) *The Radiometric Calibration of SOHO, ISSI* **SR-002**, ESA, Nordwijk, 135.

Meftah, M., Meissonnier, M., Irbah, A., Abbaki, S., Assus, P., Bertran, E., Dubois, J.P., Ducourt, E., Dufour, C., Marcovici, J.P., Poiet, G., Vieau, A.J., Thuillier, G.: 2010, *Proc. SPIE* **773**, 773145.

Mekaoui, S., Dewitte, S., Conscience, C., Chevalier, A.: 2010, *Adv. Space Res.* **45**, 1393.

Moses, D., Clette, F., Delaboudinière, J.-P., Artzner, G.E., Bougnet, M., Brunaud, J., Carabetian, C., Gabriel, A.H., Hochedez, J.F., Millier, F., Song, X.Y., Au, B., Dere, K.P., Howard, R.A., Kreplin, R., Michels, D.J., Defise, J.M., Jamar, C., Rochus, P., Chauvineau, J.P., Marioge, J.P., Catura, R.C., Lemen, J.R., Shing, L., Stern, R.A., Gurman, J.B., Neupert, W.M., Newmark, J., Thompson, B., Maucherat, A., Portier-Fozzani, F., Berghmans, D., Cugnon, P., van Dessel, E.L., Gabryl, J.R.: 1997, *Solar Phys.* **175**, 571. ADS:1997SoPh..175..571M, doi:10.1023/A:1004902913117.

Pauluhn, A., Solanki, S.K.: 2003, *Astron. Astrophys.* **407**, 359.

Pauluhn, A., Huber, M.C.E., von Steiger, R. (eds.): 2002, *The Radiometric Calibration of SOHO*, ISSI **SR-002**, ESA, Nordwijk.

Pauluhn, A., Rüedi, I., Solanki, S.K., Schühle, U., Wilhelm, K., Lang, J., Thompson, W.T., Hollandt, J.: 2001, *Appl. Opt.* **40**, 6292.

Pickles, A.J.: 1998, *Pub. Astron. Soc. Pac.* **110**, 863.

Schmutz, W., Fehlmann, A., Hüsen, G., Meindl, P., Winkler, R., Thuillier, G., Blattner, P., Buisson, F., Egorova, T., Finsterle, W., Fox, N., Gröbner, J., Hochedez, J.-F., Koller, S., Meftah, M., Meisonnier, M., Nyeki, S., Pfiffner, D., Roth, H., Rozanov, E., Spescha, M., Wehrli, C., Werner, L., Wyss, J.U.: 2009, *Metrologia* **46**, S202.

Schühle, U.: 1993, In: Silver, E.H., Kahn, S.M. (eds.) *UV and X-Ray Spectroscopy of Laboratory and Astrophysical Plasmas*, Cambridge University Press, Cambridge, 373.

Schühle, U.: 2003, In: Keil, S.L., Avakyan, S.V. (eds.) *Innovative Telescopes and Instrumentation for Solar Astrophysics, Proc. SPIE* **4853**, 88.

Schühle, U., Wilhelm, K., Hollandt, J., Paustian, W., Kühne, M.: 1994, In: *Proc. of the International Workshop on VUV and X-Ray Radiometry for Space Based Instruments*, PTB Berlin, 69.

Schühle, U., Brekke, P., Curdt, W., Hollandt, J., Lemaire, P., Wilhelm, K.: 1998, *Appl. Opt.* **37**, 2646.

Schühle, U., Thomas, R., Kent, B., Clette, F., Defise, J.-M., Delaboudinière, J.-P., Fröhlich, C., Gardner, L., Kohl, J., Hochedez, J.-F., Moses, J.D.: 2002, In: Pauluhn, A., Huber, M.C.E., von Steiger, R. (eds.) *The Radiometric Calibration of SOHO*, ISSI **SR-002**, ESA, Nordwijk, 289.

Seaton, D.B., Berghmans, D., Nicula, B., Halain, J.-P., De Groof, A., Thibert, T., Bloomfield, D.S., Raftery, C.L., Gallagher, P.T., Auchère, F., Defise, J.-M., D'Huys, R., Lecat, J.-H., Mazy, E.,

Rochus, P., Rossi, L., Schühle, U., Slemzin, V., Yalim, M.S., Zender, J.: 2012, *Solar Phys.* doi:10.1007/s11207-012-0114-6.

Sperfeld, P., Metzdorf, J., Harrison, N.J., Fox, N.P., Khlevnoy, B.B., Khromchenko, V.B., Mekhontsev, S.N., Shapoval, V.I., Zelener, M.F., Sapritsky, V.I.: 1998, *Metrologia* **35**, 419.

Thernisien, A.F., Morrill, J.S., Howard, R.A., Wang, D.: 2006, *Solar Phys.* **233**, 155. ADS:2006SoPh..233..155T, doi:10.1007/s11207-006-2047-4.

Thompson, W.T.: 1999, *Proc. SPIE* **3764**, 196.

Thompson, W.T.: 2000, *Opt. Eng.* **39**, 2651.

Thompson, W.T.: 2006, In: Lacoste, H. (ed.) *SOHO-17. 10 Years of SOHO and Beyond* **SP-617**, ESA, Nordwijk.

Thuillier, G., Foujols, T., Bolsée, D., Gillotay, D., Hersé, M., Peetermans, W., Decuyper, W., Mandel, H., Sperfeld, P., Pape, S., Taubert, D.R., Hartmann, J.: 2009, *Solar Phys.* **257**, 185. ADS:2009SoPh..257..185T, doi:10.1007/s11207-009-9361-6.

Tsuneta, S., Ichimoto, K., Katsukawa, Y., Nagata, S., Otsubo, M., Shimizu, T., *et al.*: 2008, *Solar Phys.* **249**, 167.

Wang, T., Thomas, R.J., Brosius, J.W., Young, P.R., Rabin, D.M., Davila, J.M., Del Zanna, G.: 2011, *Astrophys. J.* **197**, 32.

Wehrli, C., Fröhlich, C., Romero, J.: 1996, *Metrologia* **32**, 653.

Wilhelm, K., Curdt, W., Marsch, E., Schühle, U., Lemaire, P., Gabriel, A., *et al.*: 1995, *Solar Phys.* **162**, 189. ADS:1995SoPh..162..189W, doi:10.1007/BF00733430.

Woods, T.N., Eparvier, F.G., Hock, R., Jones, A.R., Woodraska, D., Judge, D., Didkovsky, L., Lean, J., Mariska, J., Warren, H., McMullin, D., Chamberlin, P., Berthiaume, G., Bailey, S., Fuller-Rowell, T., Sojka, J., Tobiska, W.K., Viereck, R.: 2012, *Solar Phys.* **275**, 115. ADS:2012SoPh..275..115W, doi:10.1007/s11207-009-9487-6.

Zacharias, N., Monet, D.G., Levine, S.E., Urban, S.E., Gaume, R., Wycoff, G.L.: 2004, *Bull. Am. Astron. Soc.* **36**, 1418.